

1 **Whole-rock and zircon evidence for evolution of the Late**  
2 **Jurassic high Sr/Y Zhoujiapuzi granite, Liaodong Peninsula,**  
3 **North China Craton**

4  
5 **Renyu Zeng**<sup>a, b, c \*</sup>, **Mark B. Allen**<sup>c</sup>, **Xiancheng Mao**<sup>d</sup>, **Jianqing Lai**<sup>d</sup>, **Jie Yan**<sup>a, b</sup>,  
6 **Jianjun Wan**<sup>a, b</sup>

7 <sup>a</sup> State Key Laboratory of Nuclear Resources and Environment, East China University  
8 of Technology, Nanchang, 330013, Jiangxi, China;

9 <sup>b</sup> School of Earth Sciences, East China University of Technology, Nanchang, 330013,  
10 China,

11 <sup>c</sup> Department of Earth Sciences, Durham University, Durham DH1 3LE, UK

12 <sup>d</sup> School of Geosciences and Info-Physics, Central South University, Changsha 410083,  
13 China

14

15 **Abstract:** Middle-Late Jurassic high Sr/Y granitic intrusions are extensively exposed  
16 in the Liaodong Peninsula, in the eastern part of the North China Craton (NCC).  
17 However, the genesis of the high Sr/Y signature in these intrusions has not been studied  
18 in detail. In this study, we report results of zircon U-Pb dating, Hf isotopic analysis and  
19 zircon and whole-rock geochemical data for the Late Jurassic Zhoujiapuzi granite in  
20 the middle part of the Liaodong Peninsula. The Zhoujiapuzi granite is high-K (calc-  
21 alkaline) and peraluminous in nature, with high SiO<sub>2</sub> (68.1–73.0 wt %) and Al<sub>2</sub>O<sub>3</sub>  
22 (14.5–16.8 wt %), low in TFe<sub>2</sub>O<sub>3</sub> (1.10–2.49 wt %) and MgO (0.10–0.44 wt %), and

23 with high Sr/Y (19.9–102.0) and  $\text{La}_N/\text{Yb}_N$  (14.59–80.40), characteristic of high Sr/Y I-  
24 type granite. The geochemical signatures, in combination with the presence of a large  
25 number of Paleoproterozoic inherited zircons, indicate that the Zhoujiapuzi granite was  
26 most likely derived from partial melting of the basement in the region, and specifically  
27 the Liaoji granites. The high Sr/Y signature is inherited from these source rocks. LA-  
28 ICP-MS zircon U-Pb dating of the autocryst zircons from two samples (from different  
29 localities) yielded consistent weighted average ages of  $160.7 \pm 1.1$  Ma (MSWD=1.3) and  
30  $159.6 \pm 1.1$  Ma (MSWD=1.2), with  $\epsilon_{\text{Hf}}(t)$  values in the range of -26.6– -22.8.  
31 Morphological and chemical studies on autocrystic zircon grains show that there are  
32 two stages of zircon growth, interpreted as magmatic evolution in two distinct stages.  
33 The light-CL core reflects a crystallization environment of low oxygen fugacity and  
34 high  $T_{\text{Zr-Ti}}$ ; the dark-CL rim formed with high oxygen fugacity and lower  $T_{\text{Zr-Ti}}$ . Based  
35 on the geochemical features and regional geological data, we propose that the Liaodong  
36 Peninsula in the Late Jurassic was part of a mature continental arc, with extensive  
37 melting of thick crust above the Paleo-Pacific subduction zone.

38 **Keywords:** Liaodong Peninsula; Late Jurassic; Zircon U-Pb-Hf isotopes; Two stages  
39 of crystal growth; High Sr/Y granite

## 40 1. Introduction

41 The Liaodong Peninsula is located in the northeast of the North China Craton  
42 (NCC). The northeast NCC was influenced by three main tectonic regimes in the  
43 Mesozoic, related to the subduction of the Paleo-Asian, Paleo-Pacific and Mongol-  
44 Okhotsk oceans (Tang et al., 2018). The superposition of these different regimes

45 resulted in changing tectonic and magmatic patterns over time. Middle-Late Jurassic  
46 granitic rocks are extensively exposed in the northern parts of the Liaodong Peninsula,  
47 such as the Yutun mylonitic granite, Xiaoheshan granodiorite, Heigou monzogranite  
48 (Wu et al., 2005), Wulong two-mica monzogranite (Yang et al., 2018), and Huangdi  
49 biotite monzogranite (Xue et al., 2020). Most of these rocks are characterized by high  
50 Sr /Y, and plot within the adakite field on Sr/Y-Y and  $La_N/Yb_N$ - $Yb_N$  diagrams (Wu et  
51 al., 2005a; Yang et al., 2015a, 2018).

52 The geodynamic settings and petrogenesis of adakite and geochemically similar  
53 high Sr/Y igneous rocks have been widely discussed. The high Sr/Y rocks were  
54 originally proposed to be formed by melting of young (<25 Ma) and hot subducted  
55 oceanic slab in an arc setting (Defant and Drummond, 1990). However, later studies  
56 have shown that the high Sr/Y rocks can form in both arc and non-arc settings by other  
57 processes, such as continental interior settings (Wang et al., 2007), cold subduction  
58 zones (Nakamura and Iwamori, 2013), collision or post-collision processes (Schwartz  
59 et al., 2011). In addition, numerous studies have suggested that the lower continental  
60 crust can also be the source of the high Sr/Y rocks (Gao et al., 2004; Ou et al., 2017).  
61 However, it is debated whether crustal thickening is necessary for their formation (e.g.  
62 Moyen, 2009; Kamei et al., 2009; Zhan et al., 2020). In recent years, some studies have  
63 proposed that the high Sr/Y ratio in granitic rocks can be inherited from a high Sr/Y  
64 crust source, regardless of pressure (Kamei et al., 2009; Ma et al., 2015; Zhan et al.,  
65 2020).

66 The Middle-Late Jurassic granitic rocks in the Liaodong Peninsula are commonly  
67 proposed to be the products of partial melting of thickened mafic crust with garnet in  
68 the residue (Wu et al., 2005a; Yang et al., 2015a, 2018; Tang et al., 2018). However, the  
69 source composition has not been fully considered in the petrogenesis of the high Sr/Y

70 rocks in the Liaodong Peninsula. Hence, the petrogenesis of the Middle-Late Jurassic  
71 high Sr/Y rocks needs to be re-evaluated, based on more detailed work and a  
72 consideration of possible sources. This petrogenesis is of significance for understanding  
73 the Jurassic tectonics of the Liaodong Peninsula, and the NCC in general.

74 In this paper, we examined the high Sr/Y Zhoujiapuzi granite from the Xiuyan area,  
75 in the middle of the Liaodong Peninsula. Zircons are analysed for U-Pb-Hf isotopes  
76 and trace element geochemistry, and by Raman spectroscopy. These results are  
77 integrated with whole-rock geochemistry. We focus on the zircons, because of their  
78 potential to reveal the origins of the pluton (Belousova et al., 2002; Wang et al., 2007;  
79 Breiter et al., 2014; Zhao et al., 2014), and so provide a case study for the evolution of  
80 plutonic magma systems in general. Based on observations of the CL images and  
81 chemical analysis, two zircon growth stages can be distinguished. We first determine  
82 the crystallization environments of the two zircon growth stages, and then decipher the  
83 petrogenesis, source characteristics and origin of the high Sr/Y signature of the pluton  
84 as a whole. Integrated with previous studies, our study provides insights into the  
85 tectonic evolution of the Liaodong Peninsula in the Late Jurassic.

## 86 **2. Geological setting**

87 The Zhoujiapuzi granite is located in the middle of the Liaodong Peninsula, at the  
88 northeastern margin of the NCC (Fig. 1). The Paleoproterozoic Liaohe Group and Liaoji  
89 granite are the basement in the study area. The Liaohe Group includes the Lieryu,  
90 Gaojiayu, Dashiqiao and Gaixian formations. Although stratigraphic terms are used,  
91 these rocks are metamorphic, and the group consists of leptynite, leptite, granulite,  
92 amphibolite, marble and phyllite. The protoliths of the Liaohe Group include marine

93 volcanics, clastics, carbonates and claystones. The formation age of the  
94 metasedimentary rocks in the Liaohe Group is 2.0–1.9 Ga (Wan et al., 2006; Li et al.,  
95 2015). It is in unconformable contact with the overlying strata of the Mesoproterozoic  
96 Cuocaogou Formation and Xiaoling Formation.

97 The study area experienced strong magmatic activity in the Paleoproterozoic,  
98 which can be divided into two stages of 2.2–2.1 Ga and ~ 1.85 Ga. The 2.18–2.14 Ga  
99 Liaoji granites (also called gneissic granites), which lie within an area measuring 300  
100 km × 70 km, are dominated by A- and I-type granites (Li and Zhao, 2007; Yang et al.,  
101 2016; Wang et al., 2020a). Metamorphosed volcanic rocks (leptynite, leptite and  
102 granulite) in the Liaohe Group also formed at 2.2–2.1 Ga (Li et al., 2015). The ~1.85  
103 Ga granites mainly consist of I- and S-type porphyry granites and alkaline syenites  
104 (Yang et al., 2007; Yang et al., 2015b). In addition, there were small amounts of mafic  
105 magmatic activity at ~2.17 Ga, ~2.1 Ga and ~1.8 Ga (Meng et al., 2014; Yuan et al.,  
106 2015). There are a variety of viewpoints on the Paleoproterozoic tectono-magmatic  
107 evolution in the Liaodong Peninsula, such as an intracontinental rift opening-closing  
108 model (Li et al., 2005) and an arc-continent collision model (Faure et al., 2004).

109 In the Mesozoic, the region of the Liaodong Peninsula was influenced by the  
110 circum-Pacific tectonic regime, the Mongol-Okhotsk tectonic regime and the Paleo-  
111 Asian Ocean tectonic regime. The joint influence of multiple tectonic regimes resulted  
112 in intensive magmatism during the Mesozoic (Fig. 1b). These Mesozoic magmatic  
113 rocks can be divided into three stages, namely: Triassic (233–212 Ma), Jurassic (180–  
114 156 Ma) and Early Cretaceous (131–117 Ma) (Wu et al., 2005b).

115 The Triassic magmatic rocks are less exposed, mainly alkaline rocks, diabase,  
116 diorites and granites (Wu et al., 2005b). Among them, the granites mainly have A-type  
117 affinity, and may have formed in an extensional setting (Tang et al., 2018; Wang et al.,  
118 2019). Magmatism has been related to either the subduction of the Paleo-Pacific slab,  
119 closure of the Paleo-Asian Ocean, or the collision between the NCC and the Yangtze  
120 Craton (Tang et al., 2018; Wang et al., 2019). The majority of the Jurassic magmatic  
121 rocks are monzogranite and granodiorite, which are generally calc-alkaline I-type  
122 granites, and show characteristics of adakite-like rocks. Some of them, exposed near  
123 later extensional structures, have undergone regional ductile deformation. These  
124 Jurassic magmatic rocks are generally considered to relate to the subduction of the  
125 Paleo-Pacific slab (Wu et al., 2005a; Zhai et al., 2004). In the Early Cretaceous, basic-  
126 acidic-alkaline rocks were widely developed. Among them, the granites have mainly  
127 A- and I-type affinities. These rocks are generally considered to have formed in an  
128 intense extensional environment, which is connected with either the rollback or low-  
129 angle subduction of the Paleo-Pacific slab (Wu et al., 2005c; Zheng et al., 2018).

### 130 **3. Samples and petrography**

131 The Zhoujiapuzi granite is located to the east of Xiuyan City, in the middle of the  
132 Liaodong Peninsula (Fig. 1b). It intruded into the Lieryu Formation of the Liaohu Group.  
133 Eight samples of the Zhoujiapuzi granite were collected at locations shown in Fig. 1c.

134 The Zhoujiapuzi granite is generally grey in colour and with fine-grained texture  
135 (Fig. 2a). The mineral assemblage contains K-feldspar (~50 %), quartz (~25 %),

136 plagioclase (~20 %) and biotite (~5 %) as well as accessory minerals such as zircon,  
137 ilmenite, magnetite and apatite. K-feldspar grains are euhedral or subhedral, and always  
138 exhibit cross-hatched twinning (Fig. 2b). Quartz grains are usually xenomorphic, and  
139 have indented boundaries and wavy extinction (Fig. 2b-d). Plagioclase always exhibits  
140 polysynthetic twinning and have sericitization in places (Fig. 2c). Biotite mainly fills  
141 in the interstices between the other minerals (Fig. 2c, d).

#### 142 **4. Analytical methods**

143 The cathodoluminescence (CL) images of zircon were obtained by the Chengpu  
144 geological Testing Co. Ltd, Langfang, China using the TIMA analysis. The LA-ICP-  
145 MS zircon U-Pb analyses were performed using an Agilent Technologies 7700x ICP-  
146 MS with a Teledyne Cetac Technologies Analyte Excite laser-ablation system at  
147 Nanjing FocuMS Contract Testing Co. Ltd. The analyses were carried out with a 35  $\mu\text{m}$   
148 spot size at 8 Hz repetition rate for 40 seconds. The ICP-MS detector has dual modes:  
149 pulse for lower signal, and analog for higher signal. Pulse-analog cross calibration was  
150 performed before the measurement of U-Pb isotopes, delivering a wider linear dynamic  
151 range – up to 10 orders of magnitude. For a signal of  $^{238}\text{U}$  higher than 1.2–1.4 Mio cps,  
152 equivalent zircon contains U concentrations higher than 600 ppm, and are measured in  
153 analog mode. 91500 was used as external standard. GJ-1 (600Ma, Jackson et al., 2004)  
154 and Plešovice (337Ma, Sláma et al., 2008) were treated as quality control for  
155 geochronology. During our analyses, the weighted mean age of GJ-1 and Plešovice  
156 were  $606.0 \pm 4.8$  Ma ( $n=16$ , MSWD = 0.50) and  $340.9 \pm 4.0$  Ma ( $n=7$ , MSWD = 1.0),  
157 respectively. Trace elements abundance of zircon were externally calibrated against  
158 NIST SRM 610 with Si as the internal standard. The raw ICP-MS data were processed

159 using ICPMSDataCal software (Liu et al., 2010). No common-Pb correction was  
160 applied to the data. Data reduction was completed using the Isoplot4.15 (Ludwig, 2003).  
161 The instrument description and analytical procedure are described in detail by Zeng et  
162 al. (2018).

163 The in-situ Lu-Hf isotopic analyses of zircon were performed by LA-MC-ICP-MS  
164 using a Teledyne Cetac laser-ablation system and a Nu Plasma II MC-ICP-MS at  
165 Nanjing FocuMS Contract Testing Co. Ltd. The 193 nm ArF excimer laser was focused  
166 on zircon surface with fluence of 6.0J/cm<sup>2</sup>. The ablation protocol employed a spot  
167 diameter of 50 um at 8 Hz repetition rate for 40 seconds. Three standard zircons, GJ-1,  
168 91500, and Penglai, were analysed for quality control at every ten unknown samples.  
169 In the experiment, standard zircon GJ-1, 91500, and Penglai were analyzed, and the  
170 <sup>176</sup>Hf/<sup>177</sup>Hf ratios were 0.282002–0.282013, 0.282305–0.282315 and 0.282901–  
171 0.282914 respectively, in accordance with their recommended values (GJ-1: 0.282012,  
172 Yuan et al., 2008; 91500: 0.282307 ± 0.000031, Wu et al., 2006; Penglai: 0.282906 ±  
173 0.000010, Li et al., 2010). For the calculation of εHf(t) values, we have adopted the  
174 <sup>176</sup>Lu decay constant of 1.867 × 10<sup>-11</sup> (Söderlund et al., 2004), the present-day  
175 chondritic values of <sup>176</sup>Lu/<sup>177</sup>Hf = 0.0332 and <sup>176</sup>Hf/<sup>177</sup>Hf = 0.282772 (Blichert-Toft and  
176 Albarède 1997). To calculate one-stage model ages (T<sub>DM1</sub>) relative to a depleted-mantle  
177 source, we have adopted the present-day depleted-mantle values of <sup>176</sup>Lu/<sup>177</sup>Hf =  
178 0.0384 and <sup>176</sup>Hf/<sup>177</sup>Hf = 0.28325 (Vervoort and Blichert-Toft 1999). To calculate two-  
179 stage modal ages (TDM2), ‘felsic crust’ model ages are calculated using average  
180 continental crust <sup>176</sup>Lu/<sup>177</sup>Hf = 0.015 (Griffin et al., 2004)

181 Zircon Raman analyses were carried out using an RM2000 laser Raman



182 spectrometer at the State Key Laboratory of Nuclear Resources and Environment, East  
183 China University of Technology. The selected incident wavelengths were 532 and 785  
184 nm in order to clearly identify the luminescence bands due to low concentration  
185 impurities. The beam power was 20 mW. The Leica 50× objective was employed.

186 Six fresh rock samples were selected for geochemical analysis. The elemental  
187 analyses were conducted at Analytical Chemistry & Testing Services (ALS) Chemex  
188 (Guangzhou) Ltd. Major oxides were analyzed using wave-dispersive X-ray  
189 fluorescence (XRF) (ME-XRF26). Analytical precision was better than  $\pm 0.01\%$ .  
190 Trace element abundances were measured by the lithium borate dissolution method and  
191 ICP-MS (ME-MS81). The analytical uncertainties of the rare earth element (REE) and  
192 high field strength element (HFSE) are  $<5\%$ . Analytical uncertainties are in the range  
193 of 5%–10% for the other elements. Detailed analytical procedures refer to Zhang et al.  
194 (2019) and Nash et al. (2020).

## 195 **5. Analytical results**

196 The data for major and trace elements, Raman microprobe data, zircon trace  
197 elements, zircon U-Pb ages, and zircon Hf isotopes are shown in Tables S1, S2, S3, S4  
198 and S5, respectively.

### 199 **5.1. Whole-rock major and trace element compositions**

200  $\text{SiO}_2$  contents range from 68.11 wt.% to 73.02 wt.% (average 71.71 wt.%).  
201 Contents of  $\text{Na}_2\text{O}$  and  $\text{K}_2\text{O}$  are 3.81 – 4.65 wt.% and 4.32 – 4.71 wt.%, respectively,  
202 with  $\text{Na}_2\text{O}/\text{K}_2\text{O}$  ratio of 0.82 – 1.08 and total alkalis ( $\text{Na}_2\text{O} + \text{K}_2\text{O}$ ) of 8.38 – 8.97. All

203 samples plot in the field of granite in the TAS classification except one (Fig. 3a). These  
204 samples have  $\text{Al}_2\text{O}_3$  contents of 14.49 – 16.83 wt.% (average 15.09 wt.%), CaO  
205 contents of 1.04 – 1.98 wt.% (average 1.38 wt.%) and A/CNK values of 1.05 – 1.10  
206 (average 1.07). In the A/NK – A/CNK diagram (Fig. 3b), all samples plot in the  
207 peraluminous field (Fig. 3b). The granite samples have low  $\text{TFe}_2\text{O}_3$  ( $\text{TFe}_2\text{O}_3$  = all Fe  
208 calculated as  $\text{Fe}_2\text{O}_3$ ) contents and MgO contents ranging from 1.10–2.49 wt % and  
209 0.10–0.44 wt %, respectively, with Mg# ( $\text{Mg\#}=100*\text{molar Mg}/(\text{Mg}+\text{Fe})$ ) values of 15–  
210 26.

211 The samples of the Zhoujiapuzi granite exhibit variable REEs, with total REEs  
212 ranging from 59 to 302 ppm. The  $\text{La}_\text{N}/\text{Yb}_\text{N}$  values of the Zhoujiapuzi granite range from  
213 14.59 to 80.40 (average 38.27), showing right-declined REE patterns (Fig. 4a). The  
214 samples have  $\text{Eu}/\text{Eu}^*$  of 0.62–1.94 and  $\text{Ce}/\text{Ce}^*$  of 0.94–1.16. In the primitive mantle-  
215 normalized trace element diagram (Fig. 4b), the samples show negative anomalies of  
216 HFSEs (e.g., Nb, Ta, Ti and P) and positive anomalies of La and LILEs (e.g., K, Rb,  
217 Ba, U, La, Ce). The Zhoujiapuzi granite is characterized by high contents of Sr (309–  
218 551 ppm) and low contents of Y (5.01–15.5 ppm) and Yb (0.43–1.40 ppm), with high  
219 Sr/Y ratios of 19.94–102.04 (average 65.50).

## 220 **5.2 Zircon CL images, Raman spectra and REE elements**

221 CL images of zircons from the Zhoujiapuzi granite are shown in Fig. 5. Zircons  
222 commonly have crystal sizes between 150 and 250  $\mu\text{m}$ , and have length/width ratios of  
223 2:1–4:1, with euhedral, stubby to elongate prisms. According to the CL images, most  
224 zircons show an internal division into 2 distinct domains: light-CL core and dark-CL  
225 rim. The light-CL core is characterized by bright CL intensity and widely-spaced

226 oscillatory zoning patterns. The dark-CL rim is overgrown continuously by the light-  
227 CL core and is characterized by extremely low CL emission and narrowly-spaced  
228 oscillatory zoning patterns. In addition, some zircons have inherited cores, which have  
229 corroded and rounded shapes in contact with the light-CL core, such as 1# and 37# in  
230 XY-001 and 6# and 41# in XY-008 (Fig. 5). These inherited zircons have oscillatory  
231 zoning in CL images.

232 Six light-CL core spots and six dark-CL rim spots were analyzed for Raman  
233 spectra. The light-CL cores have antisymmetric stretching vibration ( $B_{1g}$ ) of the  $SiO_4$   
234 tetrahedra ( $\nu_3$  ( $SiO_4$ )) Raman band of 1005–1007  $cm^{-1}$  and half-width of the  $\nu_3$  ( $SiO_4$ )  
235 Raman band ( $b$ ) values of 6.0–8.1  $cm^{-1}$ , while the dark-CL rims have  $\nu_3$  ( $SiO_4$ ) Raman  
236 band of 1004–1007  $cm^{-1}$  and  $b$  values of 5.4–9.0  $cm^{-1}$ .

237 Twenty light-CL core spots, eighteen dark-CL rim spots and six inherited zircon  
238 spots were analyzed for trace and rare earth elements. The light-CL core spots have  
239 lower U content (28–677 ppm) than the dark-CL rim spots (U=641–3842 ppm). In the  
240 chondrite-normalized REE element diagram (Fig. 6a, b), both the light-CL core and  
241 dark-CL rim are characterized by HREE enrichment relative to LREE with positive Ce  
242 anomalies and negative Eu anomalies. The light-CL core spots have  $\Sigma REE$  of 49–1115  
243 ppm (average 390 ppm),  $\Sigma LREE$  of 3–72 ppm (average 14 ppm) and  $\Sigma HREE$  of 46–  
244 1100 ppm (average 377 ppm), whereas the dark-CL rim spots have  $\Sigma REE$  of 327–1632  
245 ppm (average 895 ppm),  $\Sigma LREE$  of 2–14 ppm (average 6 ppm) and  $\Sigma HREE$  of 325–  
246 1627 ppm (average 889 ppm). Hence, the REE content of the light-CL core is  
247 significantly lower than that of the dark-CL rim, and the difference between the two is  
248 mainly in HREE content. The light-CL core spots have  $Eu/Eu^*$  of 0.07–0.60 (average  
249 0.28) and  $Ce/Ce^*$  of 1.89–24.27 (average 10.03). Because the contents of La and Pr are  
250 typically present very low,  $Ce^*$  in this study is obtained by the formulation  $(Nd_N)^2 / Sm_N$

251 (Loader et al., 2017). The dark-CL rim spots have  $\text{Eu}/\text{Eu}^*$  of 0.08–0.24 (average 0.13)  
252 and  $\text{Ce}/\text{Ce}^*$  of 6.57–200.31 (average 79.23). These results indicate that the light-CL  
253 core have a weaker negative Eu anomaly and a weaker positive Ce anomaly than those  
254 of the dark-CL rim. The inherited zircon spots have  $\Sigma\text{REE}$  of 602–1517 ppm, and show  
255 depletion of LREE, enrichment of HREE, a positive Ce anomaly ( $\text{Ce}/\text{Ce}^*$  of 1.52–  
256 216.08) and a negative Eu anomaly ( $\text{Eu}/\text{Eu}^*$  of 0.07–0.13) (Fig. 6c).

### 257 **5.3 Zircon U–Pb and Hf isotope composition**

258 Seventy-seven spots were analysed for U–Pb isotope composition from samples  
259 XY-001 and XY-008. In the U–Pb Concordia diagram (Fig. 7a, c), both the light-CL  
260 core and dark-CL rim spots overlap within uncertainty on the Concordia curve. There  
261 is a large degree of overlap between the dark-CL rim and light-CL core in terms of  
262  $^{206}\text{Pb}/^{238}\text{U}$  age although the mean value for  $^{206}\text{Pb}/^{238}\text{U}$  age is higher in the light-CL core  
263 (Fig. 7e). On a single zircon, the  $^{206}\text{Pb}/^{238}\text{U}$  age of the light-CL core is older than that  
264 of the dark-CL rim (Fig. 5). In sample XY-001, 33 spots define a weighted mean  
265  $^{206}\text{Pb}/^{238}\text{U}$  age of  $160.7 \pm 1.1$  Ma ( $2\sigma$ , MSWD=1.3; Fig. 7b). In sample XY-008, 28 spots  
266 define a weighted mean  $^{206}\text{Pb}/^{238}\text{U}$  age of  $159.6 \pm 1.1$  Ma ( $2\sigma$ , MSWD=1.2; Fig. 7d). The  
267 other 10 spots with distinctly older ages ( $^{207}\text{Pb}/^{206}\text{Pb}$  ages ranging from 2500 to 2173  
268 Ma) were obtained on inherited cores. Their ages are discordant, suggesting that these  
269 inherited cores were variably influenced by lead loss. Among these, 9 spots define a  
270 discordia line with an upper intercept age of  $2163 \pm 13$  Ma (MSWD=0.45) (Fig. 7f).

271 Twenty-four zircons were analyzed for Lu–Hf isotope composition. The variation  
272 in Hf isotopic data is limited, between 9 spots from light-CL core and 9 spots from dark-  
273 CL rim. 18 spots exhibit a range of  $^{176}\text{Hf}/^{177}\text{Hf}$  ratios from 0.281921 to 0.282030, which  
274 converts to  $\epsilon\text{Hf}(t)$  values between -26.6 to -22.8 (Fig. 8), and two-stage Hf model ( $T_{\text{DM}2}$ )

275 ages of 2650 to 2889 Ma by using the U-Pb age for each zircon. Six analytical spots,  
276 which define the Concordia upper intercept age of 2163 Ma, show  $^{176}\text{Hf}/^{177}\text{Hf}$  ratios  
277 and  $\epsilon\text{Hf}(t)$  values of 0.281443 to 0.281496 and -0.7 to 1.5, respectively, with  $T_{\text{DM2}}$  age  
278 of 2648 Ma to 2791 Ma by using the upper intercept age.

## 279 **6. Discussion**

### 280 **6.1 Significance of the two stages of zircon**

281 Generally, zircon with high U content can easily break down into the metamict  
282 state because of the radiation damage to the lattice caused by  $\alpha$ -particles originating  
283 from the decay of uranium (Mezger and Krogstad, 1997). The physical and structural  
284 changes often lead to the loss of Pb and addition of trace elements such as LREE. In  
285 this study, the dark-CL rim spots have high U content, which is significantly higher than  
286 the median value of zircon U content in granitic magma (350 ppm, Wang et al., 2011).  
287 Hence, the metamictization degree of the zircons must be taken into consideration. Data  
288 from dark-CL rim spots plot on the Concordia curve, indicating no obvious Pb loss. The  
289 internal structure of dark-CL rim is relatively intact, with obvious oscillatory zoning,  
290 and few cracks, implying that the physical and structural of the dark-CL rim remained  
291 unchanged. Nasdala et al. (1998) suggested that the metamictization of zircon can be  
292 well characterized by Raman spectroscopy. The half-width of the  $\nu_3(\text{SiO}_4)$  Raman band  
293 ( $b$ ) of  $10\text{ cm}^{-1}$  and  $20\text{ cm}^{-1}$  are proposed to approximately distinguish well-crystallized,  
294 intermediate and metamict zircons (Nasdala et al., 1998). The dark-CL rim have  $b$   
295 values of 5.4–9.2, characterizing them as well-crystallized. Therefore, the above

296 features indicate that the dark-CL rim are not metamict. Consequently, it can be  
297 concluded that the U-Pb isotope and trace element systematics of the dark-CL rim have  
298 not been changed by metamictization.

299 Both the light-CL core and dark-CL rim have oscillatory zoning patterns, and their  
300 chondrite-normalized REE patterns are characterized by steeply positive slopes from  
301 the LREE to HREE with strong negative Eu anomalies and pronounced positive Ce  
302 anomalies. The above characteristics are consistent with those of igneous zircon  
303 (Hoskin and Schaltegger, 2003). Although hydrothermal zircon can also have  
304 oscillatory zoning patterns similar to magmatic zircons, there are obvious differences  
305 in trace elements between the magmatic and hydrothermal zircon (Hoskin et al., 2005).  
306 In the discrimination diagram (Fig. 9), both the spots of light-CL core and dark-CL rim  
307 fall in or near the magmatic field, which is obviously different from hydrothermal  
308 zircon. Hence, the above characteristics indicate that both the light-CL core and dark-  
309 CL rim have a magmatic origin.

310 The light-CL core was overgrown continuously by the dark-CL rim. In addition,  
311 the contact between the light-CL core and dark-CL rim is euhedral. Such core-mantle  
312 overgrowth relationships indicate that the light-CL core domains are not inherited  
313 zircons. The similar Hf isotopic data of the light-CL core and dark-CL rim is also  
314 consistent with this interpretation. For the age population, the samples of XY-001 and  
315 XY-008 have MSWD of 1.3 and 1.2, respectively, which are both within the expected  
316 range for 95 % confidence interval (Mahon, 1996). Although the  $^{206}\text{Pb}/^{238}\text{U}$  age of dark-  
317 CL rim is generally younger than that of light-CL core, the ages of these two distinct

318 domains have the characteristics of continuous variation, and do not show two or more  
319 distinct age populations (Fig. 7b, d). These phenomena do not support the presence of  
320 antecrystic zircons (Siégel et al., 2018). Hence, both the light-CL core and dark-CL rim  
321 are most likely autocrystic zircon formed in one distinct pulse of magma. The weighted  
322 mean U-Pb ages of  $160.7\pm 1.1$  Ma and  $159.6\pm 1.1$  Ma can be interpreted as the  
323 emplacement age of the Zhoujiapuzi granite. The obvious difference in internal  
324 structure and trace element composition between the light-CL core and dark-CL rim  
325 could be due to significant changes in their crystallization environments (Wang et al.,  
326 2007).

327 The Zr/Hf ratio in zircon has a negative correlation with the degree of fractionation  
328 in the parent melt (Claiborne et al., 2006). In this study, the Zr/Hf ratios of the dark-CL  
329 rim (21–40) are obviously lower than those of the light-CL core (39–56) (Fig. 10a). In  
330 addition, incompatible elements such as U and REE will become enriched in the highly  
331 evolved magma (Zhao et al., 2014). In this study, the contents of U and REE of dark-  
332 CL rim are significantly higher than those of light-CL core (Fig. 10a). Overall, the  
333 above features reflect that the dark-CL rim crystallized from a later and more evolved  
334 magma.

335 Watson and Harrison (2005) found that the Ti content of zircon has a strong  
336 dependence on temperature (T), and obtained a Ti-in-zircon thermometer ( $T_{Zr-Ti}$ ). Since  
337 then, Ferry and Watson (2007) suggested that the solubility of Ti in zircon depends not  
338 only on T and activity of  $TiO_2$  ( $a_{TiO_2}$ ) but also on the activity of  $SiO_2$  ( $a_{SiO_2}$ ), and  
339 revised the  $T_{Zr-Ti}$ . We use the  $T_{Zr-Ti}$  from Ferry and Watson (2007) and the recommended

340 values ( $a_{\text{SiO}_2}=1$ ,  $a_{\text{TiO}_2} = 0.5$ ) for the activity of  $\text{SiO}_2$  and  $\text{TiO}_2$  (Schiller and Finger,  
341 2019), due to the presence of ilmenite and quartz in the Zhoujiapuzi granite. The  $T_{\text{Zr-Ti}}$   
342 from the light-CL core and dark-CL rim are 684–830 °C (average 761 °C) and 509–  
343 712°C (average 635 °C), respectively, i.e. the light-CL core formed at higher  
344 temperatures than the dark-CL rim. The  $T_{\text{Zr-Ti}}$  value shows a significant positive  
345 correlation with  $\text{Zr/Hf}$  (a tracer of fractional crystallisation), and shows continual  
346 fractionation and cooling (Fig. 10b). As the light-CL core and dark-CL rim formed in  
347 different magmatic evolution stages, it is problematic to use the same  $a_{\text{SiO}_2}$  and  $a_{\text{TiO}_2}$   
348 values to calculate both  $T_{\text{Zr-Ti}}$  values for both. For ilmenite bearing granites, Schiller  
349 and Finger (2019) suggested that the variation of  $a_{\text{TiO}_2}$  values corresponding to  
350 different zircon crystallization stages is small. In addition, Schiller and Finger (2019)  
351 showed that the  $a_{\text{SiO}_2}$  value of the ilmenite-bearing granites at the onset of magmatic  
352 zircon crystallization was more than 0.75. Even if the  $a_{\text{SiO}_2}$  value of the light-CL core  
353 is changed from 1.0 to 0.75, the temperature will only drop by about ~27 °C, which is  
354 significantly lower than the 126 °C difference between the average  $T_{\text{Zr-Ti}}$  value of the  
355 light-CL core and dark-CL rim. Therefore, it is certain that the light-CL core formed at  
356 higher temperatures than the dark-CL rim, although we cannot calculate the specific  
357 temperature difference.

358 Cerium exists in magmas as both  $\text{Ce}^{3+}$  and  $\text{Ce}^{4+}$ . Because the 0.84-Å radius of the  
359  $\text{Zr}^{4+}$  ion is more closely matched by the  $\text{Ce}^{4+}$  (0.97-Å radius) than the  $\text{Ce}^{3+}$  (1.143-Å  
360 radius) (all ionic radii are from Shannon, 1976),  $\text{Ce}^{4+}$  is more compatible in the zircon  
361 structure than the  $\text{Ce}^{3+}$ . Hence, the magnitude of Ce anomaly is a useful tool for



362 evaluating the oxygen fugacity condition of crystallization environment (e.g. Ballard et  
363 al., 2002; Trail et al., 2012). Loader et al. (2017) suggested that the Ce/Ce\* ratio is  
364 likely to be the most robust measure of magma redox conditions, although it is only a  
365 semi-quantitative measure. In this study, the Ce/Ce\* ratio of the light-CL core and dark-  
366 CL rim are 6.30–153.36 (average 32.51) and 21.81–5773.06 (average 787.39),  
367 respectively. This result suggests that the dark-CL rim formed in a higher oxygen  
368 fugacity environment than the light-CL core. As shown in the Ce/Ce\*-Zr/Hf diagram  
369 (Fig. 10c), Ce/Ce\* has a significant negative correlation with Zr/Hf, showing that the  
370 oxygen fugacity condition is increasing with the evolution of magma.

371 The absence of enclaves and disequilibrium textures in the Zhoujiapuzi granite  
372 and uniform  $\epsilon_{\text{Hf}}(t)$  values of the light-CL core and dark-CL rim do not support magma  
373 mixing and wall-rock assimilation. Consequently, the abrupt change between the  
374 crystallization environment of the light-CL core and dark-CL rim is not due to the  
375 magma mixing or contamination during magma evolution. Therefore, we propose that  
376 the light-CL core was formed in a relatively deep magma chamber, which had low  
377 oxygen fugacity, low Zr saturation and higher temperature. The low Th, U and REE,  
378 and widely-spaced oscillatory zoning patterns indicate a low growth rate of zircon  
379 (Hoskin and Schaltegger, 2003; Wang et al., 2011). In contrast, the dark-CL rim was  
380 formed during the ascent and/or at the emplacement location of the magma. At this  
381 stage, the oxygen fugacity significantly increased, the temperature decreased, and Zr  
382 saturation increased due to the crystallization differentiation. In this environment, the  
383 crystallization rate of zircon significantly increased, forming the zircons with a higher

384 content of Th, U and REE elements, low CL emission and narrowly-spaced oscillatory  
385 zoning patterns.

386 Zircon U-Pb dating is the most commonly used method in geochronology,  
387 especially dating the emplacement age of magmatic rocks. A weighted mean age or  
388 upper intercept age is usually obtained to represent the emplacement time of a magmatic  
389 rock. However, the autocrystic zircons in this study record two different magmatic  
390 evolution stages. Previous studies, such as Wang et al. (2007), Zhao et al. (2014) and  
391 Chen et al. (2020), also show that zircons can crystallize continually or intermittently  
392 in a single phase of magmatism, showing several growth zones of clearly different  
393 internal structure and distinct time difference. Therefore, autocrystic zircon can be  
394 formed in two or more evolution stages during one distinct pulse or increment of  
395 magma. Some scholars even regard that the age difference of different stages can be  
396 more than dozens of Ma (Wang et al., 2007). Therefore, if the zircon ages in the same  
397 magmatic rock have a large range of variation, this could be caused by the zircons  
398 recording different stages in magmatic evolution, related to different levels of magma  
399 within the crust and/or different temperature regimes. In this paper, although the  
400 apparent age of the dark-CL rim is generally younger than that of the light-CL core, the  
401 age difference between the two is within the error range of the in-situ LA-ICP-MS  
402 analyses (individual spot of  $\pm 3\text{--}5\%$  relative precision, Schmitz and Kuiper, 2013).  
403 Therefore, further work is needed to verify the actual age difference between the two  
404 magmatic evolution stages. Nevertheless, it is notable that the bulk petrology and  
405 geochemistry of the host pluton does not record and reveal this two-stage magmatic

406 evolution, which can only be detected in the zircon analysis.

## 407 **6.2 Genetic type: I-type affinity**

408 The Zhoujiapuzi granite has low Zr (113 - 242 ppm), Ce (26.5 - 121.5 ppm),  
409 Zr+Nb+Ce+Y (152.0 - 382.6 ppm), (Na<sub>2</sub>O + K<sub>2</sub>O)/CaO (4.53 - 8.31) and FeO\*/MgO  
410 (5.09 - 10.56), distinct from the typical A-type granites (Fig. 11a-d). Furthermore, the  
411 Zhoujiapuzi granite does not contain mafic alkaline minerals, such as arfvedsonite,  
412 riebeckite, etc., which is also distinctly inconsistent with typical A-type granites (Wu et  
413 al., 2003). Wu et al. (2017) suggested that a high formation temperature is one of the  
414 most important characteristics of A-type granite. Zircon saturation thermometry ( $T_{Zrn}$ )  
415 and Ti-in-zircon thermometer ( $T_{Zr-Ti}$ ) are two methods for estimating magma  
416 temperatures. As noted above, because the values of  $a_{SiO_2}$  and  $a_{TiO_2}$  during the early  
417 zircon crystallization cannot be accurately obtained, the temperature of this period  
418 cannot be accurately obtained through the Ti-in-zircon thermometer. Zircon saturation  
419 thermometry was introduced by Watson and Harrison (1983) and is suitable for non-  
420 peralkaline crustal source rocks. Since the zircon solubility is mainly affected by  
421 temperature, major element compositions have a limited impact on calculated  $T_{Zrn}$   
422 (Miller et al., 2003). In addition, the errors introduced by crystal-rich composition tend  
423 to cancel as changes in Zr concentration and M value during crystallization have  
424 opposite effects on the  $T_{Zrn}$  value (Miller et al., 2003). Therefore, the composition of  
425 Zhoujiapuzi granite can be used to estimate the magma temperature. The calculated  $T_{Zrn}$   
426 values for the Zhoujiapuzi granite are in the range of 803-870 °C (mean=845 ±20°C).

427 It was proposed that the  $T_{Zm}$  suggests an upper limit on the temperature of melt  
428 generation for inheritance-rich granitoid (Miller et al., 2003). Hence, the magma  
429 temperature of the Zhoujiapuzi granite should be lower than or equal to the  $T_{Zm}$  value,  
430 which is significantly lower than that of typical A-type granite ( $>900$  °C, Skjerlie and  
431 Johnston, 1992; Douce, 1997). Thus, the Zhoujiapuzi granite is not an A-type granite.

432 The samples of the Zhoujiapuzi granite have  $A/KNC < 1.1$ , relatively high  $Na_2O$   
433 (3.96–4.65 wt.%) and lack peraluminous minerals (e.g. cordierite, andalusite,  
434 muscovite and garnet), which are clearly different from S-type granites (Chappell and  
435 White, 1992). With the rise of the degree of crystallization,  $P_2O_5$  contents  
436 (generally  $>0.1$  wt.%) increase in S-type granites, accompanied by an  
437 increase/immunity in  $SiO_2$  (Wolf and London, 1994). However, the Zhoujiapuzi  
438 granite samples have low  $P_2O_5$  contents (0.02 – 0.08 wt.%), and decrease with  
439 increasing  $SiO_2$  (Fig. 11e), which are features consistent with the I-type granite rather  
440 than S-type granite (Chappell and White, 1992). Additionally, Rb has a positive  
441 correlation with Y (Fig. 11f), which has been considered as an indicator of I-type granite  
442 (Jiang et al., 2018). Furthermore, the composition of the Zhoujiapuzi granite fall in the  
443 I-type granite field in the discrimination diagrams of granites introduced by Collins et  
444 al. (1982) (Fig. 11 c-d). Therefore, we conclude that the Zhoujiapuzi granite is a I-type  
445 granite.

### 446 **6.3 Petrogenesis of the high Sr/Y granite**

447 The samples of the Zhoujiapuzi granite have high Sr/Y and  $(La/Yb)_N$  ratios and  
448 low Y and Yb contents (Fig. 12a) consistent with the geochemical signatures of modern

449 adakites (Defant and Drummond, 1990). However, other geochemical parameters of  
450 the Zhoujiapuzi granite, such as the high  $K_2O/Na_2O$  ratio (0.93 –1.22), low  $Al_2O_3$   
451 content (14.49 –15.02%, except one) and Sr content (in half of the samples lower than  
452 400 ppm), are obviously different from typical adakites ( $K_2O/Na_2O \leq 0.42$ ,  $Al_2O_3 \geq$   
453 15 %, Sr>400 ppm, Defant and Drummond., 1990; Drummond et al., 1996, Martin et  
454 al., 2005). A variety of petrogenetic models have been proposed for the origin of high  
455 Sr/Y magmatic rocks, such as partial melting of subducting oceanic crust (Model A,  
456 Defant and Drummond, 1990), delaminated lower continental crust (LCC) (Model B,  
457 Kay and Kay, 1993; Xu et al., 2002), differentiation of basaltic arc magma (Model C,  
458 Castillo et al., 1999), magma mixing between mantle-derived mafic and crust-derived  
459 silicic magmas (Model D, Ma et al., 2013a), partial melting of thickened basaltic LCC  
460 (Model E, Gao et al., 2004; Ou et al., 2017), or melting of a high Sr/Y (and La/Yb)  
461 source (Model F, Kamei et al., 2009; Ma et al., 2015).

### 462 **6.3.1 Model A: Partial melting of subducting oceanic crust**

463 The partial melting of the young, hot and hydrated subducted oceanic slab in the  
464 garnet stability field is the classical formation model of adakite (high Sr/Y rock) (Defant  
465 and Drummond, 1990). Studies have shown that the rock with this genetic model  
466 generally has the characteristics of high mantle components (such as MgO, CaO and  
467 Cr) because of the involvement of mantle magma (Wang et al., 2018). However, this  
468 phenomenon was not seen in the Zhoujiapuzi granite. In addition, the Zhoujiapuzi  
469 granite has high  $K_2O/Na_2O$  ratios (0.92–1.22, average 1.13), which is inconsistent with  
470 the slab-derived adakites ( $K_2O/Na_2O = \sim 0.4$ , Martin et al., 2005). Moreover, the low  
471  $\epsilon_{Hf}(t)$  values (-26.6 to -22.8) of the Zhoujiapuzi granite are also inconsistent with the  
472 magmas derived from the partial melting of oceanic crust, which generally have

473 depleted isotopic character (Zhan et al., 2020). Furthermore, the Zhoujiapuzi granite  
474 has low Ti/Eu and high Nd/Sm ratios (Fig. 13a), and markedly negative Nb-Ta  
475 anomalies (Fig. 4b), which are distinct from those of oceanic basalts (Yu et al., 2012).  
476 In summary, the Zhoujiapuzi granite is difficult to explain by Model A.

### 477 **6.3.2 Model B: Delaminated lower continental crust (LCC)**

478 High-density, garnet-bearing mafic lower crust delaminating or foundering into  
479 the asthenosphere mantle and subsequent interaction with mantle peridotite could  
480 produce high Sr/Y magmas (Kay and Kay 1993). Because the melt formed by partial  
481 melting of the delaminated lower crust would interact with mantle peridotite during  
482 magma ascent, the high Sr/Y magmas related to this petrogenetic model generally have  
483 high MgO, Mg# and TiO<sub>2</sub> (Gao et al., 2004; Ou et al., 2017; He et al., 2021). The MgO  
484 (0.10– 0.44 wt.%), Mg# (15– 26) and TiO<sub>2</sub> (0.09– 0.34 wt.%) values of Zhoujiapuzi  
485 granite are significantly lower than the above values (Fig. 13b- d). In addition,  
486 delamination of the lower crust generally occurs in within-plate extensional settings  
487 (Gao et al., 2004), and will form a large number of Mg-rich (Mg#>50) rocks due to the  
488 partial melting of lithospheric mantle and/or upwelling of asthenosphere (Ou et al.,  
489 2017). However, these Jurassic magmatic rocks in the Liaodong Peninsula are generally  
490 considered to be formed in a compressional environment related to the subduction of  
491 the Paleo-Pacific slab (Li et al., 2004; Yang et al., 2015a; Zhu and Xu, 2019; Zheng et  
492 al., 2018). Furthermore, the middle-late Jurassic granites are generally Mg-poor (Fig.  
493 13c). Due to the high temperature of the asthenosphere (1200 °C, Parsons and  
494 McKenzie, 1978; King et al., 2015), rocks formed by partial melting of the delaminated  
495 lower crust should possess a high-temperature fingerprint. T<sub>Zm</sub> has been used as a  
496 geothermometer to estimate partial melting temperatures (e.g., Miller et al., 2003;

497 Collins et al., 2016). As mentioned before, the  $T_{Zrn}$  of the Zhoujiapuzi granite is below  
498 900 °C, which is markedly lower than the temperature of the asthenosphere. Therefore,  
499 the petrogenetic model of delaminated lower continental crust (Model B) is also  
500 inconsistent with the Zhoujiapuzi granite.

### 501 **6.3.3 Model C: Differentiation of basaltic arc magma**

502 Low-pressure fractional crystallization (involving olivine + clinopyroxene +  
503 plagioclase + amphibole+ titanomagnetite) or high-pressure fractional crystallization  
504 (involving garnet) from basaltic magmas have been proposed as two ways to generate  
505 adakitic characteristics (Castillo et al., 1999; Macpherson et al., 2006).

506 However, the composition of the Zhoujiapuzi granite is relatively uniform,  
507 including SiO<sub>2</sub>, MgO and Na<sub>2</sub>O, which does not support major fractional crystallization  
508 (Xue et al., 2017). Furthermore, the Zhoujiapuzi granite has abundant inherited zircons  
509 and no obvious depletion of Sr, Eu and Ba, showing that this granite has not experienced  
510 extensive fractionation (Miller et al., 2003). The samples form clear partial melting  
511 trends on the La/Yb versus La diagram (Fig. 13e), which also suggests that partial  
512 melting was more important than fractional crystallization (Gao et al., 2007; Shahbazi  
513 et al., 2021). In addition, crystal fractionation of basaltic melts can only form minor  
514 volumes of granitic melts, the ratio of the two is about 9:1 (Zeng et al., 2016). However,  
515 for the same age interval, no coexisting mafic-intermediate rocks have been found in  
516 the research area. In the wider region of the Liaodong Peninsula, Middle-Late Jurassic  
517 magmatism is dominated by felsic compositions; mafic- intermediate rocks are only  
518 reported in the Huaziyu area (lamprophyre dikes, Jiang et al., 2005). Therefore, it is  
519 unlikely that there are large-scale mafic- intermediate rocks contemporaneous with the  
520 Zhoujiapuzi granite at depth according to the rock assemblage of Liaodong Peninsula

521 in this period. Moreover, the zircon Hf isotopic compositions of the Zhoujiapuzi granite  
522 are quite different from those of the depleted mantle, but are similar to those of the  
523 basement (Liaohu Group and Liaoji granite) in the study area (Fig. 8). The ancient  
524 inherited zircons (2500 to 2173) with low  $\epsilon\text{Hf}(t)$  values also indicate older crustal  
525 material in the Zhoujiapuzi granite. For these reasons, it is highly improbable that  
526 Zhoujiapuzi granite was derived by differentiation of basaltic magma (Model C).

#### 527 **6.3.4 Model D: Magma mixing between mantle-derived mafic and crust-derived** 528 **silicic magmas**

529 The Zhoujiapuzi granite has high  $\text{K}_2\text{O}/\text{Na}_2\text{O}$  ratio ( $>1$ ) and  $A/\text{CNK}$  value ( $>1$ ),  
530 together with the absence of mingling textures, mafic microgranular enclaves (MMEs),  
531 felsic xenocrysts and melting texture of plagioclase, implying that the mantle-derived  
532 magma is unlikely to have played an important role in the genesis of the Zhoujiapuzi  
533 granite (Castro et al., 1991). In addition, the Zhoujiapuzi granite is characterized by the  
534 development of biotite, but lacks amphibole and pyroxene. These features, coupled with  
535 the high  $A/\text{CNK}$  value, are consistent with an origin as a crust-derived granitoid, but  
536 obviously different from the granitoids formed by crust-mantle-derived magma mixing  
537 (Barbarin, 1990). Moreover, granites formed by magma mixing generally have high  
538  $\text{MgO}$ ,  $\text{TFe}_2\text{O}_3$ ,  $\text{CaO}$  and  $\text{Cr}$  contents and low  $\text{SiO}_2$  content (Ma et al., 2013a; Wang et  
539 al., 2018). These features are obviously inconsistent with the Zhoujiapuzi granite in this  
540 study. Additionally, the  $\epsilon\text{Hf}(t)$  values and trace element composition of the two stages  
541 of zircon also do not support magma mixing. Hence, magma mixing of mantle-derived  
542 and crust-derived magmas (Model D) is also unlikely to have produced the Zhoujiapuzi  
543 granite.



### 544 **6.3.5 Model E: Partial melting of thickened basaltic LCC**

545 Experimental studies have shown that the partial melt of basaltic LCC in the garnet  
546 stabilization zone (> 40 km, i.e. ~1.2 GPa) can produce magma with a high Sr/Y ratio  
547 (Rapp et al., 2003 and references therein). In these scenarios, high Sr/Y and overall  
548 adakitic affinity are caused by leaving garnet as residual phases (e.g. Gao et al., 2004).  
549 Based on geochemical data for the Zhoujiapuzi granites, partial melting of thickened  
550 basaltic LCC is also unlikely to account for the high Sr/Y Zhoujiapuzi granite (Model  
551 E). This conclusion is based on the following observations:

552 (1) This ratio of  $(\text{Gd}/\text{Yb})_{\text{N}}$  is the most important feature to judge whether garnet is  
553 involvement in magma genesis (Ma et al., 2012). If the  $(\text{Gd}/\text{Yb})_{\text{N}}$  ratio of the source is  
554 similar to the average value of the LCC (1.71, Rudnick and Gao, 2003), partial melting  
555 of these crustal materials controlled by garnet at high pressure can produce melt with  
556  $(\text{Gd}/\text{Yb})_{\text{N}}$  of 5.8 (Huang and He, 2010). In contrast, the  $(\text{Gd}/\text{Yb})_{\text{N}}$  values (1.22–5.06,  
557 average 2.69) of the Zhoujiapuzi granite are relatively low. (2) Studies of lower-crustal  
558 xenoliths show that garnet may not be a common mineral in the lower crust of the NCC  
559 (Ma et al., 2012). (3) As shown in the discrimination diagrams of granite sources (Fig.  
560 13f, g), all samples fall in the range of metagreywacke-derived melts. Therefore, the  
561 Zhoujiapuzi granite was considered to have been derived from crustal anatexis of  
562 metagraywacke (or intermediate-acid igneous rock with similar mineral composition),  
563 rather than basaltic lower crust.

### 564 **6.3.6 Model F: Melting of a high Sr/Y (and La/Yb) source**

565 Studies have shown that when a source rock has a high Sr/Y ratio, the high Sr/Y  
566 signature of the derived magma can inherit from their source, regardless of pressure  
567 (Kamei et al., 2009; Moyen, 2009; Ma et al., 2015). We suggest that partial melting of

568 high Sr/Y Liaoji granite was most probably the origin of the high Sr/Y Zhoujiapuzi  
569 granite, as discussed below (Model F).

570 The Zhoujiapuzi granite has similar mineral assemblages (contains abundant K-  
571 feldspar and lacks hornblende) and geochemical composition (Fig. 13h) to the  
572 Tsutsugatake intrusion, which is explained by partial melting of arc-type tonalite or  
573 adakitic granodiorite (Kamei et al., 2009). Among the inherited zircons from  
574 Zhoujiapuzi granite, the  $^{207}\text{Pb} / ^{206}\text{Pb}$  ages of all the spots are between 2132 and 2200  
575 Ma, except one, and yield a Concordia upper intercept age of 2163 Ma. Both  
576 assimilation of country-rocks and incomplete melting of source rocks can explain the  
577 genesis of inherited zircon in granite. Due to the similar  $T_{\text{DM2}}$  of autocrystic zircons  
578 (light-CL core and dark-CL rim) and inherited zircons, these inherited zircons most  
579 likely come from the source of the Zhoujiapuzi granite. In the study area, meta-  
580 sedimentary rocks and meta-volcanic rocks of the South Liaohe Group,  
581 Paleoproterozoic mafic rocks, as well as the Liaoji granites, have  $\sim 2.16$  Ga zircon. In  
582 spite of an age peak of 2.17–2.16 Ga in detrital zircon age spectra of the metasediments  
583 from the South Liaohe Group, melting of a sediment-dominated source is unlikely to  
584 have occurred, as it would have also introduced other age peaks such as  $\sim 2.03$  Ga and  
585  $\sim 2.50$  Ga (Li et al., 2015; Wang et al., 2020b). In addition, given the I-type  
586 characteristics of the Zhoujiapuzi granite, derivation from an igneous precursor is more  
587 plausible rather than a metasedimentary origin (Chappell and White, 1992). Therefore,  
588 these  $\sim 2.16$  Ga zircons from the Zhoujiapuzi granite are unlikely to come from the  
589 South Liaohe Group. As shown in the host rock discrimination diagrams (Fig. 14,  
590 introduced by Belousova et al., 2002), all the  $\sim 2.16$  Ga inherited zircons from  
591 Zhoujiapuzi granite fall into the granitoid area (Fig. 14), precluding that these  $\sim 2.16$  Ga  
592 zircon come from the Paleoproterozoic mafic rocks. In addition, the  $\sim 2.16$  Ga inherited

593 zircons from Zhoujiapuzi granite and the zircons from the Liaoji granites lie in a similar  
594 area in the  $\epsilon\text{Hf}(t)$ -age (Ma) diagram (Fig. 8). Hence, the  $\sim 2.16$  Ga inherited zircon most  
595 likely come from the Liaoji granites.

596 Some of the Liaoji granites, such as the Muniuhe granite (comprising granodiorite  
597 and syenogranite with no distinct boundary between the two), have adakitic signatures,  
598 and similar REE and trace element patterns as the Zhoujiapuzi granite (Fig. 4). Based  
599 on a model of batch melting (Shaw, 1970) using the experiments of Conrad et al. (1988),  
600 the high Sr/Y characteristic of the Zhoujiapuzi granite can be explained by partial  
601 melting of Muniuhe granitic pluton leaving amphibole as the main residue (Fig. 12b).

602 In our modelling, we choose the XY-005 sample to approximately represent the  
603 primitive melt composition. The reasons are as below: as mentioned above, the high  
604 Sr/Y characteristics of the Zhoujiapuzi granite are not caused by the fractional  
605 crystallization of amphibole. Furthermore, the lack of positive correlation between  
606  $\text{D}_{\text{Y}}/\text{Yb}_{\text{N}}$  ratios and  $\text{La}_{\text{N}}/\text{Yb}_{\text{N}}$  ratios (Fig. 13i) also suggests that fractional  
607 crystallization of amphibole was not a significant process for the Zhoujiapuzi granite.  
608 On the other hand, the samples of Zhoujiapuzi granite display variable Eu and Sr  
609 contents, implying that plagioclase is likely a fractional phase. The separation of  
610 titanomagnetite could explain the positive trend in  $\text{TFe}_2\text{O}_3$  with increasing  $\text{TiO}_2$  content,  
611 consistent with the occurrences of magnetite in some studied rocks. This possible  
612 mineral assemblage of fractional crystallization is also reflected by the chemical  
613 variations in the Sr/Y-Y diagram (Fig. 12b). Hence, the sample XY-005, which has  
614 highest Sr/Y, was chosen to represent a primitive melt composition. To find the best  
615 matching experimental melts, we have compared the major elements of the XY-005  
616 sample with that of experimental melts and the characteristics of no garnet residue  
617 discussed above. Results are shown in Fig. 12b. The Sr and Y compositions of the

618 starting material used in these experiments resemble those of the average composition  
619 of the Muniuhe granitic pluton (Sr=475 ppm, Y=9.77 ppm), if the residue contains a  
620 large volume of amphibole (>90 %). However, if more plagioclase is retained in the  
621 residue (e.g. 18.3 %), a source region with a higher Sr content is required. Therefore, a  
622 similar high Sr/Y Liaoji granite to the Muniuhe granitic pluton can produce the high  
623 Sr/Y signatures of the Zhoujiapuzi granite.

624 A large number of Yanshanian adakites (or high Sr/Y rocks) are developed in the  
625 NCC, which are generally considered to be derived from the thickened basaltic LCC  
626 (e.g. Gao et al., 2004; Wu et al., 2005a; Ma et al., 2013b). Zhang et al. (2001, 2003)  
627 suggested that these so-called “C-type adakites” indicated a large-scale crustal  
628 thickening event. However, according to the studies on the Triassic and Jurassic adakitic  
629 rocks near the Pingquan area, the northern part of the NCC, Ma et al. (2012, 2015)  
630 suggested that the adakitic signatures of these rocks are inherited from their source  
631 rocks. The research of the Zhoujiapuzi granite in this study also shows that among the  
632 widely distributed Jurassic high Sr/Y granites in the Liaodong Peninsula, there is at  
633 least one pluton with a high Sr/Y signature inherited from the source. Therefore, we  
634 suggest that melting of a high Sr/Y (and La/Yb) source is one of the important processes  
635 for the generation of Yanshanian high Sr/Y rocks in the NCC. This kind of high Sr/Y  
636 granite does not need to be formed in the garnet stability field.

#### 637 **6.4 Tectonic implications**

638 A large number of Early Jurassic arc-like igneous rocks occur in the northeast part  
639 of NCC- Korean Peninsula-Hida belt, which belong to the middle-high K calc-alkaline  
640 series and are characterized by enrichment in LILE and depletions in HFSE (Wu et al.,  
641 2007; Tang et al., 2018 and references therein). In addition, the Early Jurassic

642 accretionary complexes in the eastern margin of the Eurasian continent and the Japan  
643 islands, such as the Heilongjiang complex, the Khabarovsk complex and the Mino-  
644 Tamba complex, are considered to be related to subduction (Wu et al., 2007; Tang et al.,  
645 2018 and references therein). It is generally accepted that the Paleo-Pacific slab  
646 subducted westwards in the Early Jurassic (Tang et al., 2018; Zhu and Xu, 2018).

647 In the middle-late Jurassic, I-type granites are dominant in the Liaodong Peninsula,  
648 such as the Zhoujiapuzi granite (this study), Heigou pluton, Gaoliduntai pluton (Wu et  
649 al., 2005a), Waling granite (Yang et al., 2015a) and Wulong granite (Yang et al., 2018).  
650 There are not A-type granites, and mantle derived magmatism is extremely rare. These  
651 granites were formed by partial melting of crustal materials without obvious  
652 contribution of mantle derived magma (Wu et al., 2005a; Yang et al., 2015b, 2018; Xue  
653 et al., 2020). In addition, WNW-ESE compression during 157-143 Ma was widespread  
654 in the Liaodong Peninsula (Yang et al., 2004; Zhang et al., 2020). It not only  
655 mylonitized the granite plutons in middle-lower crust levels, but also intensely  
656 deformed the thick sedimentary cover in the upper crust (Qiu et al., 2018; Ren et al.,  
657 2020). Hence, Late Jurassic magmatism in the Liaodong peninsula is most likely to be  
658 related to subduction of the Paleo-Pacific plate in a mature continental arc, with crust  
659 previously thickened by compressional tectonics, related to both the oceanic subduction  
660 and the earlier Mesozoic collisions at the north and south margins of the NCC. This  
661 setting would produce the conditions required for extensive crustal melting of pre-  
662 existing basement. There is a potential resemblance to the modern arc of the Central  
663 Andes (Allmendinger et al., 1997), where crustal thickening and plateau growth has

664 developed over the Cenozoic (Scott et al., 2018), and melting of older basement has  
665 taken place during subduction of the Nazca plate (Miller and Harris, 1989). This model  
666 is also consistent with the idea that much of eastern China was a high orogenic plateau  
667 during the Mesozoic, before widespread Early Cretaceous extension and core complex  
668 development (Meng, 2003; Chu et al., 2020).

## 669 **7. Conclusions**

670 (1) LA-ICP-MS zircon U-Pb dating indicates that the Zhoujiapuzi granite in the  
671 Liaodong Peninsula formed at ~160 Ma.

672 (2) Zircon growth in Zhoujiapuzi granite can be divided into two distinct stages.  
673 The light-CL core was formed in a deeper, hotter, magma chamber, which had low  
674 oxygen fugacity and high temperature. The dark-CL rim formed from later, more  
675 evolved, magma. Oxygen fugacity significantly increased and the temperature  
676 decreased at this stage. The Zhoujiapuzi granite is a case study of multistage generation  
677 and emplacement of magma, revealed by zircons, where no signals are discernible in  
678 the bulk petrology or geochemistry.

679 (3) The I-type Zhoujiapuzi granite originated from partial melting of the  
680 Paleoproterozoic Liaoji granites. The high Sr/Y compositions are inherited from their  
681 source rocks, rather than being a direct indication of deep crustal melting, or any other  
682 common mechanism for generating adakitic signatures.

683 (4) The Late Jurassic tectonic setting of the Liaodong Peninsula and the eastern  
684 NCC resembled the modern orogenic plateau of the Central Andes, where silicic

685 magmatism may occur by partial melting of older continental crust in a compressional  
686 environment, related to the subduction of the Paleo-Pacific plate.

### 687 **Acknowledgements**

688 We thank Dr. Wenzhou Xiao, Dr. Jiajie Chen and Dr. Quan Ou for constructive reviews  
689 and useful suggestions. We are also grateful to Ying Liu, Chunying Guo, Jianxiong Hu,  
690 Ziming Hu for their help with the field work. This research was funded by the National  
691 Nature Science Foundation of China (Grants No. 42030809, 41772349, 41902075,  
692 42002095; 42162013), China Scholarship Council (No. 202008360018), Geological  
693 Exploration Program of China Nuclear Geology (Grant No. D1802), the research grants  
694 from the East China University of Technology (Grant No. DHBK2017103), Open  
695 Research Fund Program of State Key Laboratory of Nuclear Resources and  
696 Environment (East China University of Technology) (Grant 2020NRE13).

### 697 **References**

- 698 Allmendinger, R. W., Jordan, T. E., Kay, S. M., and Isacks, B. L.: The evolution of the  
699 Altiplano-Puna plateau of the Central Andes, *Annu. Rev. Earth Pl. Sc.*, 25, 139–  
700 174, <https://doi.org/10.1146/annurev.earth.25.1.139>, 1997.
- 701 Altherr, R., Holl, A., Hegner, E., Langer, C. and Kreuzer, H.: High-potassium, calc-  
702 alkaline I-type plutonism in the European Variscides: northern Vosges (France)  
703 and northern Schwarzwald (Germany), *Lithos*, 50(1-3), 51–73,  
704 [https://doi.org/10.1016/S0024-4937\(99\)00052-3](https://doi.org/10.1016/S0024-4937(99)00052-3), 2000.
- 705 Ballard, J. R., Palin, M. J., and Campbell, I. H.: Relative oxidation states of magmas

706 inferred from Ce(IV)/Ce(III) in zircon: application to porphyry copper deposits of  
707 northern Chile. *Contrib. Mineral. Petrol.*, 144, 347–364,  
708 <https://doi.org/10.1007/s00410-002-0402-5>, 2002.

709 Barbarin, B.: Granitoids: main petrogenetic classification in relation to origin and  
710 tectonic setting, *Geol. J.*, 25, 227–238, 1990.

711 Belousova, E., Griffin, W., O'Reilly, S. Y., and Fisher, N.: Igneous zircon: trace  
712 element composition as an indicator of source rock type, *Contrib. Mineral. Petrol.*,  
713 143, 602–622, <https://doi.org/10.1007/s00410-002-0364-7>, 2002.

714 Blichert-Toft, J., and Albarède, F.: The Lu-Hf isotope geochemistry of chondrites and  
715 the evolution of the mantle-crust system, *Earth. Planet. Sc. Lett.*, 148(1), 243–258,  
716 [https://doi.org/10.1016/S0012-821X\(97\)00040-X](https://doi.org/10.1016/S0012-821X(97)00040-X), 1997.

717 Breiter, K., Lamarão, C. N., Borges, R. M. K., and Dall'Agnol, R.: Chemical  
718 characteristics of zircon from A-type granites and comparison to zircon of S-type  
719 granites, *Lithos*, 192–195, 208–225, <https://doi.org/10.1016/j.lithos.2014.02.004>,  
720 2014.

721 Castillo, P. R., Janney, P. E., and Solidum, R. U.: Petrology and geochemistry of  
722 Camiguin Island, southern Philippines: Insights to the source of adakites and other  
723 lavas in a complex arc setting, *Contrib. Mineral. Petrol.*, 134(1), 33–51,  
724 <https://doi.org/10.1007/s004100050467>, 1999.

725 Castro, A., Moreno-Ventas, I., and Rosa, J.: H-type (hybrid) granitoids: a proposed  
726 revision of the granite-type classification and nomenclature, *Earth. Sci. Rev.*, 31,  
727 237–253, [https://doi.org/10.1016/0012-8252\(91\)90020-G](https://doi.org/10.1016/0012-8252(91)90020-G), 1991.



728 Chappell, B. W., and White, A. J. R.: I-and S-type granites in the Lachlan Fold Belt,  
729 Geol. Soc. Am. Spec. Pap., 272, 1–26, <https://doi.org/10.1130/SPE272-p1>, 1992.

730 Chen, S. R., Wang, Q., Zhu, D. C., Weinberg, R. F., Zhang, L. L., and Zhao, Z. D.:  
731 Reheating and magma mixing recorded by zircon and quartz from high-silica  
732 rhyolite in the Coqen region, southern Tibet, Am. Miner.,  
733 <https://doi.org/10.2138/am-2020-7426>, 2020.

734 Chu, Y., Lin, W., Faure, M., Allen, M. B., and Feng, Z.: Cretaceous exhumation of the  
735 Triassic intracontinental Xuefengshan Belt: Delayed unroofing of an orogenic  
736 plateau across the South China Block? Tectonophysics, 793, 228592,  
737 <https://doi.org/1016/j.tecto.2020.228592>, 2020.

738 Claiborne, L. L., Miller, C. F., Walker, B. A., Wooden, J. L., Mazdab, F. K., and Bea,  
739 F.: Tracking magmatic processes through Zr/Hf ratios in rocks and Hf and Ti  
740 zoning in zircons: An example from the Spirit Mountain batholith, Nevada.  
741 Mineral. Mag., 70, 517–543, <https://doi.org/10.1180/0026461067050348>, 2006.

742 Collins, W. J., Beams, S. D., White, A. J. R., and Chappell, B. W.: Nature and origin  
743 of A-type granites with particular reference to southeastern Australia, Contrib.  
744 Mineral. Petr., 80, 189-200, <https://doi.org/10.1007/BF00374895>, 1982.

745 Collins, W. J., Huang, H. Q., and Jiang, X. Y.: Water-fluxed crustal melting produces  
746 Cordilleran batholiths, Geology, 44(2), 143–146,  
747 <https://doi.org/10.1130/G37398.1>, 2016.

748 Conrad, W. K., Nicholls, I. A., and Wall, V. J.: Water-saturated and -undersaturated  
749 melting of metaluminous and peraluminous crustal compositions at 10 kb:

750 evidence for the origin of silicic magmas in the Taupo Volcanic Zone, New  
751 Zealand, and other occurrences, *J. Petrol.*, 29, 765–803,  
752 <https://doi.org/10.1093/petrology/29.4.765>, 1988.

753 Defant, M. J., and Drummond, M. S.: Derivation of some modern arc magmas by  
754 melting of young subducted lithosphere, *Nature*, 347, 662–665,  
755 <https://doi.org/10.1038/347662a0>, 1990.

756 Douce, A. E. P.: Generation of metaluminous A-type granites by low-pressure melting  
757 of calc-alkaline granitoids, *Geology*, 25, 743–746, [https://doi.org/10.1130/0091-  
758 7613\(1997\)025<0743:GOMATG>2.3.CO;2](https://doi.org/10.1130/0091-7613(1997)025<0743:GOMATG>2.3.CO;2), 1997.

759 Drummond, M. S., Defant, M. J., and Kepezhinskas, P. K.: Petrogenesis of slab-derived  
760 trondhjemite–tonalite–dacite/adakite magmas, *Trans. R. Soc. Edinb.*, 87, 205–215,  
761 <https://doi.org/10.1017/S0263593300006611>, 1996.

762 Faure, M., Lin, W., Moni, P., and Bruguier, O.: Paleoproterozoic arc magmatism and  
763 collision in Liaodong Peninsula, NE China, *Terra. Nova.*, 16, 75–80,  
764 <https://doi.org/10.1111/j.1365-3121.2004.00533.x>, 2004.

765 Ferry, J. M., and Watson, E. B.: New thermodynamic models and revised calibrations  
766 for the Ti-in-zircon and Zr-in-rutile thermometers, *Contrib. Mineral. Petrol.*, 154,  
767 429–437, <https://doi.org/10.1007/s00410-007-0201-0>, 2007.

768 Frost, B. R., Barnes, C. G., Collins, W. J., Arculus, R. J., Ellis, D. J., and Frost, C. D.:  
769 A geochemical classification for granitic rocks, *J. Petrol.*, 42, 2033–2048,  
770 <https://doi.org/10.1093/petrology/42.11.2033>, 2001.

771 Gao, S., Rudnick, R. L., Yuan, H. L., Liu, X. M., Liu, Y. S., Xu, W. L., Ling, W. L.,

772 Ayers, J. C., Wang, X. C., and Wang, Q. H.: Recycling lower continental crust in  
773 the North China craton, *Nature*, 432, 892–897,  
774 <https://doi.org/10.1038/nature03162>, 2004.

775 Gao, Y. F., Hou, Z. Q., Kamber, B. S., Wei, R. H., Meng, X.J., and Zhao, R. S.: Adakite-  
776 like porphyries from the southern Tibetan continental collision zones: evidence for  
777 slab melt metasomatism, *Contrib. Mineral. Petr.*, 153, 105–20, 10.1007/s00410-  
778 006-0137-9, 2007.

779 Griffin, W. L., Belousova, E. A., Shee, S. R., Pearson, N. J., and O'Reilly, S. Y.:  
780 Archean crustal evolution in the northern Yilgarn Craton: U-Pb and Hf-isotope  
781 evidence from detrital zircons, *Precambrian. Res.*, 131, 231–282,  
782 <https://doi.org/10.1016/J.PRECAMRES.2003.12.011>, 2004.

783 He, P. L., Huang, X. L., Yang, F., and Wang, X.: Mineralogy constraints on magmatic  
784 processes controlling adakitic features of Early Permian high-magnesium diorites  
785 in the Western Tianshan orogenic belt, *J. Petrol.*, 61, a114,  
786 <https://doi.org/10.1093/petrology/egaa114>, 2021.

787 Hoskin, P. W. O.: Trace-element composition of hydrothermal zircon and the alteration  
788 of Hadean zircon from the Jack Hills, Australia, *Geochim. Cosmochim. Ac.*, 69,  
789 637–648, <https://doi.org/10.1016/j.gca.2004.07.006>, 2005.

790 Hoskin, P. W., and Schaltegger, U.: The composition of zircon and igneous and  
791 metamorphic petrogenesis, *Rev. Mineral. Geochem.*, 53, 27–62,  
792 <https://doi.org/10.2113/0530027>, 2003.

793 Huang, F., and He, Y.S.: Partial melting of the dry mafic continental crust: Implications

794 for petrogenesis of C-type adakites, Chinese. Sci. Bull., 55, 1255–1267,  
795 <https://doi.org/10.1007/s11434-010-3224-2>, 2010.

796 Jackson, S. E., Pearson, N. J., Griffin W L, and Belousova, E. A.: The application of  
797 laser ablation-inductively coupled plasma-mass spectrometry to in situ U-Pb  
798 zircon geochronology, Chem. Geol., 211(1-2), 47–69,  
799 <https://doi.org/doi:10.1016/j.chemgeo.2004.06.017>, 2004.

800 Jiang, H., Jiang, S. Y., Li, W. Q., Zhao, K. D., and Peng, N. J.: Highly fractionated  
801 Jurassic I-type granites and related tungsten mineralization in the Shirenzhang  
802 deposit, northern Guangdong, South China: Evidence from cassiterite and zircon  
803 U-Pb ages, geochemistry and Sr-Nd-Pb-Hf isotopes, Lithos, S480187509,  
804 <https://doi.org/10.1016/j.lithos.2018.04.030>, 2018.

805 Jiang, Y.H., Jiang, S.Y., Zhao, K.D., Ni, P., Ling, H.F., and Liu, D.Y.: SHRIMP U-Pb  
806 zircon dating for lamprophyre from Liaodong Peninsula: Constraints on the initial  
807 time of Mesozoic lithosphere thinning beneath eastern China, Chinese. Sci. Bull.,  
808 50, <https://doi.org/10.1360/982005-373>, 2612–2620, 2005.

809 Kamei, A., Miyake, Y., Owada, M., and Kimura, J.: A pseudo adakite derived from  
810 partial melting of tonalitic to granodioritic crust, Kyushu, southwest Japan arc,  
811 Lithos, 112, 615–625, <https://doi.org/10.1016/j.lithos.2009.05.024>, 2009.

812 Kay, R. W., and Kay, S. M.: Delamination and delamination magmatism,  
813 Tectonophysics, 219, 177–189, [https://doi.org/10.1016/0040-1951\(93\)90295-U](https://doi.org/10.1016/0040-1951(93)90295-U),  
814 1993.

815 King, S. D., Frost, D. J., and Rubie D. C.: Why cold slabs stagnate in the transition zone,

816 Geology, 43(3), 231–234, <https://doi.org/10.1130/G36320.1>, 2015.

817 Li, C.M., Zhang, C.H., Cope, T.D., and Lin, Y.: Out-of-sequence thrusting in polycyclic  
818 thrust belts: An example from the Mesozoic Yanshan belt, North China Craton,  
819 Tectonics, 35, 2082–2116, <https://doi.org/10.1002/2016TC004187>, 2016.

820 Li, S. Z., and Zhao, G. C.: SHRIMP U-Pb zircon geochronology of the Liaoji granitoids:  
821 Constraints on the evolution of the Paleoproterozoic Jiao-Liao-Ji belt in the  
822 Eastern Block of the North China Craton, Precambrian. Res., 158, 1–16,  
823 <https://doi.org/10.1016/j.precamres.2007.04.001>, 2007.

824 Li, S. Z., Zhao, G. C., Sun, M., Han, Z. Z., Hao, D. F., Luo, Y., and Xia, X. P.:  
825 Deformation history of the Paleoproterozoic Liaohe Group in the Eastern Block  
826 of the North China Craton, J. Asian. Earth. Sci., 24, 659–674, [https://doi.org/659–](https://doi.org/659-67410.1016/j.jseaes.2003.11.008)  
827 [67410.1016/j.jseaes.2003.11.008](https://doi.org/67410.1016/j.jseaes.2003.11.008), 2005.

828 Li, S.Z., Liu, J.Z., Zhao, G.C., Wu, F.Y., Han, Z.Z., and Yang, Z.Z.: Key  
829 geochronology of Mesozoic deformation in the eastern block of the North China  
830 Craton and its constraints on regional tectonics: A case of Jiaodong and Liaodong  
831 Peninsula, Acta. Petrol. Sin., 2, 633–646, <https://doi.org/10.1007/BF02873097>,  
832 2004.

833 Li, X.H., Long, W.G., Li, Q.L., Liu, Y., Zheng, Y.F., Yang, Y.H., Chamberlain, K.R.,  
834 Wan, D.F., Guo, C.H., and Wang, X.C.: Penglai Zircon Megacrysts: A Potential  
835 New Working Reference Material for Microbeam Determination of Hf-O Isotopes  
836 and U-Pb Age, Geostand. Geoanal. Res., 34, 117–134,  
837 <https://doi.org/info:doi/10.1111/j.1751-908X.2010.00036.x>, 2010.

838 Li, Z., Chen, B., Liu, J.W., Zhang, L., and Yang, C.: Zircon U-Pb ages and their  
839 implications for the South Liaohe Group in the Liaodong Peninsula, Northeast  
840 China (in Chinese with English abstract), *Acta. Petrol. Sin.*, 31(6), 1589–1605,  
841 2015.

842 Liu, Y.S., Hu, Z.C., Zong, K.Q., Gao, C.G., Gao, S., Xu, J., and Chen, H.H.:  
843 Reappraisal and refinement of zircon U-Pb isotope and trace element analyses  
844 by LA-ICP-MS, Chinese. *Sci. Bull.*, 55, 1535–1546,  
845 <https://doi.org/10.1007/s11434-010-3052-4>, 2010.

846 Loader, M. A., Wilkinson, J. J., and Armstrong, R. N.: The effect of titanite  
847 crystallisation on Eu and Ce anomalies in zircon and its implications for the  
848 assessment of porphyry Cu deposit fertility, *Earth. Planet. Sc. Lett.*, 472, 107–119,  
849 <https://doi.org/10.1016/j.epsl.2017.05.010>, 2017.

850 Ludwig, K. R.: User's manual for Isoplot 3.00: a geochronological toolkit for Microsoft  
851 Excel, Berkeley. Geochronology. Center., 2003.

852 Ma, L., Jiang, S.Y., Dai, B.Z., Jiang, Y.H., Hou, M.L., Pu, W., and Xu, B.: Multiple  
853 sources for the origin of Late Jurassic Linglong adakitic granite in the Shandong  
854 Peninsula, eastern China: Zircon U-Pb geochronological, geochemical and Sr-Nd-  
855 Hf isotopic evidence, *Lithos*, 162–163, 251–263,  
856 <https://doi.org/10.1016/j.lithos.2013.01.009>, 2013b.

857 Ma, Q., Zheng, J.P., Griffin, W. L., Zhang, M., Tang, H.Y., Su, Y.P., and Ping, X.Q.:  
858 Triassic “adakitic” rocks in an extensional setting (North China): Melts from the  
859 cratonic lower crust, *Lithos*, 149, 159–173, <https://doi.org/>

860 10.1016/j.lithos.2012.04.017, 2012.

861 Ma, Q., Zheng, J.P., Xu, Y.G., Griffin, W. L., and Zhang, R.S.: Are continental  
862 “adakites” derived from thickened or foundered lower crust? *Earth. Planet. Sc.*  
863 *Lett.*, 419, 125–133, <https://doi.org/10.1016/j.epsl.2015.02.036>, 2015.

864 Ma, X.H., Chen, B., and Yang, M.C.: Magma mixing origin for the Aolunhua porphyry  
865 related to Mo-Cu mineralization, eastern Central Asian Orogenic Belt, Gondwana.  
866 *Res.*, 24, 1152–1171, <https://doi.org/10.1016/j.gr.2013.02.010>, 2013a.

867 Macpherson, C. G., Dreher, S. T., and Thirlwall, M. F.: Adakites without slab melting:  
868 High pressure differentiation of island arc magma, Mindanao, the Philippines,  
869 *Earth. Planet. Sc. Lett.*, 243(3), 581–593,  
870 <https://doi.org/10.1016/j.epsl.2005.12.034>, 2006.

871 Mahon, K. I.: The New “York” regression: Application of an improved statistical  
872 method to geochemistry, *Int. Geol. Rev.*, 38(4), 293–303,  
873 <https://doi.org/10.1080/00206819709465336>, 1996.

874 Maniar, P. D., and Piccoli, P. M.: Tectonic discrimination of granitoids, *Geol. Soc. Am.*  
875 *Bull.*, 101, 635–643, [https://doi.org/10.1130/0016-](https://doi.org/10.1130/0016-7606(1989)101<0635:TDOG>2.3.CO;2)  
876 [7606\(1989\)101<0635:TDOG>2.3.CO;2](https://doi.org/10.1130/0016-7606(1989)101<0635:TDOG>2.3.CO;2), 1989.

877 Martin, H., Smithies, R.H., Rapp, R., Moyen, J.-F., and Champion, D.: An overview of  
878 adakite, tonalite-trondhjemite-granodiorite (TTG), and sanukitoid: relationships  
879 and some implications for crustal evolution, *Lithos*, 79, 1–24,  
880 <https://doi.org/10.1016/j.lithos.2004.04.048>, 2005.

881 Meng, E., Liu, F.L., Liu, P.H., Liu, C.H., Yang, H., Wang, F., Shi, J.R., and Cai, J.:

882 Petrogenesis and tectonic significance of Paleoproterozoic meta-mafic rocks from  
883 central Liaodong Peninsula, northeast China: Evidence from zircon U-Pb dating  
884 and in situ Lu-Hf isotopes, and whole-rock geochemistry, *Precambrian. Res.*, 247,  
885 92–109, <https://doi.org/10.1016/j.precamres.2014.03.017>, 2014.

886 Meng, Q. R.: What drove late Mesozoic extension of the northern China-Mongolia tract?  
887 *Tectonophysics*, 369, 155–174, [https://doi.org/10.1016/S0040-1951\(03\)00195-1](https://doi.org/10.1016/S0040-1951(03)00195-1),  
888 2003.

889 Mezger, K., and Krogstad, E. J.: Interpretation of discordant U-Pb zircon ages: An  
890 evaluation, *J. Metamorph. Geol.*, 15, 127–140, [https://doi.org/10.1111/j.1525-  
891 1314.1997.00008.x](https://doi.org/10.1111/j.1525-1314.1997.00008.x), 1997.

892 Miller, C. F., McDowell, S. M., and Mapes, R. W.: Hot and cold granites? Implications  
893 of zircon saturation temperatures and preservation of inheritance, *Geology*, 31,  
894 529–532, [https://doi.org/10.1130/0091-7613\(2003\)031<0529:hacgio>2.0.co;2](https://doi.org/10.1130/0091-7613(2003)031<0529:hacgio>2.0.co;2),  
895 2003.

896 Miller, J.F., and Harris, N.B.W.: Evolution of continental crust in the Central Andes;  
897 constraints from Nd isotope systematics, *Geology*, 17, 615–617,  
898 [https://doi.org/10.1130/0091-7613\(1989\)0172.3.CO;2](https://doi.org/10.1130/0091-7613(1989)0172.3.CO;2), 1989.

899 Moyen, J.: High Sr/Y and La/Yb ratios: The meaning of the “adakitic signature”, *Lithos*,  
900 112, 556–574, <https://doi.org/10.1016/j.lithos.2009.04.001>, 2009.

901 Nakamura, H., and Iwamori, H.: Generation of adakites in a cold subduction zone due  
902 to double subducting plates, *Contrib. Mineral. Petr.*, 165, 1107–1134,  
903 <https://doi.org/10.1007/s00410-013-0850-0>, 2013.



904 Nasdala, L., Pidgeon, R. T., Wolf, D., and Irmer, G., Metamictization and U-Pb isotopic  
905 discordance in single zircons: a combined Raman microprobe and SHRIMP ion  
906 probe study, *Miner. Petrol.*, 62, 1–27, <https://doi.org/10.1007/BF01173760>, 1998.

907 Nash, D.J., Ciborowski, T., Ullyott, J.S., Pearson, M.P. and Whitaker, K.A.: Origins of  
908 the sarsen megaliths at Stonehenge, *Sci. Adv.*, 6, eabc0133,  
909 <https://doi.org/10.1126/sciadv.abc0133>, 2020.

910 Ou, Q., Wang, Q., Wyman, D. A., Zhang, H.X., Yang, J.H., Zeng, J.P., Hao, L.L., Chen,  
911 Y.W., Liang, and H., Qi, Y.: Eocene adakitic porphyries in the central-northern  
912 Qiangtang Block, central Tibet: Partial melting of thickened lower crust and  
913 implications for initial surface uplifting of the plateau, *J. Geophys. Res. Solid.*  
914 *Earth.*, 122, 1025–1053, <https://doi.org/10.1002/2016JB013259>, 2017.

915 Parsons, B., and Dan, M.K.: Mantle convection and the thermal structure of the plates,  
916 *J. Geophys. Res. Solid. Earth.*, 83, <https://doi.org/10.1029/JB083iB09p04485>,  
917 1978.

918 Patiño Douce, A.E.P.: What do experiments tell us about the relative contributions of  
919 crust and mantle to the origin of granitic magmas? *Geol. Soc. Lond. Spec. Publ.*,  
920 168(1), 55–75, <https://doi.org/10.1144/GSL.SP.1999.168.01.05>, 1999.

921 Qiu, L., Kong, R.Y., Yan, D.P., Wells, M.L., Wang, A.P., Sun, W.H., Yang, W.X., Han,  
922 Y.G., Li, C.M., and Zhang, Y.X.: The Zhayao tectonic window of the Jurassic  
923 Yuantai thrust system in Liaodong Peninsula, NE China: Geometry, kinematics  
924 and tectonic implications, *J. Asian Earth Sci.*, 164, 58–71, [https://doi.org/](https://doi.org/10.1016/j.jseaes.2018.06.012)  
925 [10.1016/j.jseaes.2018.06.012](https://doi.org/10.1016/j.jseaes.2018.06.012), 2018.

926 Rapp, R. P., Shimizu, N and Norman, M.D.: Growth of early continental crust by partial  
927 melting of eclogite, *Nature*, 425(6958), 605–609,  
928 <https://doi.org/10.1038/nature02031>, 2003.

929 Ren, Z.H., Lin, W., Faure, M., Meng, L.T., Qiu, H.B., and Zeng, J.P.: Triassic- Jurassic  
930 evolution of the eastern North China Craton: Insights from the Lushun-Dalian area,  
931 South Liaodong Peninsula, NE China, *Geol. Soc. Am. Bull.*, 133(1–2),  
932 <https://doi.org/10.1130/B35533.1>, 2020.

933 Rudnick, R. L., and Gao, S.: Composition of the continental crust, *Treatise. Geochem.*,  
934 3, 1–64, <https://doi.org/10.1016/b0-08-043751-6/03016-4>, 2003.

935 Schiller, D., and Finger, F.: Application of Ti-in-zircon thermometry to granite studies:  
936 problems and possible solutions, *Contrib. Mineral. Petr.*, 174,  
937 <https://doi.org/10.1007/s00410-019-1585-3>, 2019.

938 Schmitz, M. D., and Kuiper, K. F.: High-Precision Geochronology, *Elements.*, 9, 25–  
939 30, <https://doi.org/10.2113/gselements.9.1.25>, 2013.

940 Schwartz, J. J., Johnson, K., Miranda, E. A., and Wooden, J. L.: The generation of high  
941 Sr/Y plutons following Late Jurassic arc–arc collision, Blue Mountains province,  
942 NE Oregon, *Lithos*, 126, 22–41, <https://doi.org/10.1016/j.lithos.2011.05.005>,  
943 2011.

944 Scott, E.M., Allen, M.B., Macpherson, C.G., McCaffrey, K.J.W., Davidson, J.P.,  
945 Saville, C., and Ducea, M.N.: Andean surface uplift constrained by radiogenic  
946 isotopes of arc lavas, *Nat. Commun.*, 9(1), 969, [https://doi.org/10.1038/s41467-](https://doi.org/10.1038/s41467-018-03173-4)  
947 [018-03173-4](https://doi.org/10.1038/s41467-018-03173-4), 2018.

948 Shahbazi, H., Maghami, Y. T., Azizi, H., Asahara, Y., Siebel, Y., Maanijou, M., and  
949 Rezaei, A.: Zircon U-Pb ages and petrogenesis of late Miocene adakitic rocks from  
950 the Sari Gunay gold deposit, NW Iran, *Geol. Mag.*,  
951 <https://doi.org/10.1017/S0016756821000297>, 2021.

952 Shannon, R.D.: Revised effective ionic radii and systematic studies of interatomic  
953 distances in halides and chalcogenides, *Acta. Crystall. A.*, 32(5), 751–767,  
954 <https://doi.org/10.1107/S0567739476001551>, 1976.

955 Shaw, D.M.: Trace element fractionation during anatexis, *Geochim. Cosmochim. Ac.*,  
956 34, 237–243, [https://doi.org/10.1016/0016-7037\(70\)90009-8](https://doi.org/10.1016/0016-7037(70)90009-8), 1970.

957 Siégel, C., Bryan, S. E., Allen, C. M., and Gust, D. A.: Use and abuse of zircon-based  
958 thermometers: A critical review and a recommended approach to identify  
959 antecrystic zircons, *Earth. Sci. Rev.*, 176, 87–116,  
960 <https://doi.org/10.1016/j.earscirev.2017.08.011>, 2018.

961 Skjerlie, K. P., and Johnston, A. D.: Vapor-absent melting at 10 kbar of a biotite-and  
962 amphibole-bearing tonalitic gneiss: implications for the generation of A-type  
963 granites, *Geology*, 20, 263–266, [https://doi.org/10.1130/0091-7613\(1992\)0202.3.CO;2](https://doi.org/10.1130/0091-7613(1992)0202.3.CO;2), 1992.

965 Sláma, J., Košler, J., and Condon, D. J.: Plešovice zircon-A new natural reference  
966 material for U-Pb and Hf isotopic microanalysis, *Chem. Geol.*, 249(1–2), 1–35,  
967 <https://doi.org/doi:10.1016/j.chemgeo.2007.11.005>, 2008.

968 Söderlund, U., Patchett, P.J., Vervoort, J.D., and Isachsen, C.E.: The 176 Lu decay  
969 constant determined by Lu-Hf and U-Pb isotope systematics of Precambrian mafic

970 intrusions, *Earth. Planet. Sc. Lett.*, 219(3), 311–324,  
971 [https://doi.org/10.1016/S0012-821X\(04\)00012-3](https://doi.org/10.1016/S0012-821X(04)00012-3), 2004.

972 Sun, S. S., and McDonough, W. F.: Chemical and isotopic systematics of oceanic  
973 basalts: implications for mantle composition and processes, *Geol. Soc. Lond. Spec.*  
974 *Publ.*, 42, 313–345, <https://doi.org/10.1144/GSL.SP.1989.042.01.19>, 1989.

975 Tang, J., Xu, W. L., Wang, F., and Ge, W.C.: Subduction history of the Paleo-Pacific  
976 slab beneath Eurasian continent: Mesozoic-Paleogene magmatic records in  
977 Northeast Asia, *Sci. China. Earth. Sci.*, 61, 527–559,  
978 <https://doi.org/CNKI:SUN:JDXG.0.2018-05-003>, 2018.

979 Trail, D., Watson, E. B., and Tailby, N. D.: Ce and Eu anomalies in zircon as proxies  
980 for the oxidation state of magmas, *Geochim. Cosmochim. Ac.*, 97, 70–87,  
981 <https://doi.org/10.1016/j.gca.2012.08.032>, 2012.

982 Vervoort, J.D., and Blichert-Toft, J.: Evolution of the depleted mantle: Hf isotope  
983 evidence from juvenile rocks through time, *Geochim. Cosmochim. Ac.*, 63(3),  
984 533–556, [https://doi.org/10.1016/S0016-7037\(98\)00274-9](https://doi.org/10.1016/S0016-7037(98)00274-9), 1999.

985 Wan, Y.S., Song, B., Liu, D.Y., Wilde, S. A., Wu, J.S., Shi, Y.R., Yin, X.Y., and Zhou,  
986 H.Y.: 2006. SHRIMP U-Pb zircon geochronology of Palaeoproterozoic  
987 metasedimentary rocks in the North China Craton: Evidence for a major Late  
988 Palaeoproterozoic tectonothermal event, *Precambrian. Res.*, 149, 271,  
989 <https://doi.org/10.1016/j.precamres.2006.06.006>, 2006.

990 Wang, F., Liu, F., Schertl, H.P., Xu, W., Liu, P., and Tian, Z.: Detrital zircon U-Pb  
991 geochronology and Hf isotopes of the Liaohe Group, Jiao-Liao-Ji Belt:

992 Implications for the Paleoproterozoic tectonic evolution, *Precambrian. Res.*, 340,  
993 105633, [10.1016/j.precamres.2020.105633](https://doi.org/10.1016/j.precamres.2020.105633), 2020b.

994 Wang, N., Wu, C. L., Lei, M., and Chen, H.J.: Petrogenesis and tectonic implications of  
995 the Early Paleozoic granites in the western segment of the North Qilian orogenic  
996 belt, China, *Lithos*, 312–313, 89–107, <https://doi.org/10.1016/j.lithos.2018.04.023>,  
997 2018.

998 Wang, Q., Xu, J. F., Jian, P., Bao Z. W., Zhao. Z. H., Li. C. F., Xiong. X. L., and Ma,  
999 J. L.: Petrogenesis of adakitic porphyries in an extensional tectonic setting, Dexing,  
1000 South China: Implications for the genesis of porphyry copper mineralization, *J.*  
1001 *Petrol.*, 47(1), 119–144, <https://doi.org/10.1093/petrology/egi070>, 2006.

1002 Wang, X. P., Oh, C. W., Peng, P., Zhai, M. G., Wang, X. H., and Lee, B. Y.:  
1003 Distribution pattern of age and geochemistry of 2.18-2.14 Ga I- and A-type  
1004 granites and their implication for the tectonics of the Liao-Ji belt in the North  
1005 China Craton, *Lithos*, 364–365, 105518,  
1006 <https://doi.org/10.1016/j.lithos.2020.105518>, 2020a.

1007 Wang, X., Griffin, W. L., Chen, J., Huang, P.Y., and Li, X.: U and Th contents and  
1008 Th/U ratios of zircon in felsic and mafic magmatic rocks: Improved zircon-melt  
1009 distribution coefficients, *Acta. Geol. Sin. Engl.*, 85, 164–174,  
1010 <https://doi.org/10.1111/j.1755-6724.2011.00387.x>, 2011.

1011 Wang, X., Griffin, W. L., O'Reilly, S. Y., and Li, W.X.: Three stages of zircon growth  
1012 in magmatic rocks from the Pingtan Complex, eastern China, *Acta. Geol. Sin.*  
1013 *Engl.*, 81, 68–80, <https://doi.org/10.3321/j.issn:1000-9515.2007.01.008>, 2007.

1014 Wang, X.L., Lv, X., Liu, Y.J., Zhao, Y.Y., Li, C., Wu, W.B., Wang, Y.P., and Li, H.Y.:  
1015 LA-ICP-MS zircon U-Pb ages, geochemical characteristics of Late Triassic  
1016 intrusives in Xiuyan area, eastern Liaoning and their geological significances, *Ore.*  
1017 *Geol. Rev.*, 65, 401–416, <https://doi.org/10.16509/j.georeview.2019.02.010>, 2019.

1018 Watson, E. B., and Harrison, T. M.: Zircon saturation revisited: temperature and  
1019 composition effects in a variety of crustal magma types, *Earth. Planet. Sci. Lett.*,  
1020 64, 295–304, [https://doi.org/10.1016/0012-821X\(83\)90211-X](https://doi.org/10.1016/0012-821X(83)90211-X), 1983.

1021 Watson, E. B., and Harrison, T. M.: Zircon thermometer reveals minimum melting  
1022 conditions on earliest Earth, *Science*, 308, 841–844,  
1023 <https://doi.org/10.1126/science.1110873>, 2005.

1024 Whalen, J. B., Currie, K. L., and Chappell, B. W.: A-type granites: geochemical  
1025 characteristics, discrimination and petrogenesis, *Contrib. Mineral. Petr.*, 95, 407–  
1026 419, <https://doi.org/10.1007/BF00402202>, 1987.

1027 Wolf, M. B., and London, D.: Apatite dissolution into peraluminous haplogranitic melts:  
1028 An experimental study of solubilities and mechanisms, *Geochim. Cosmochim.*  
1029 *Acta.*, 58, 4127–4145. [https://doi.org/10.1016/0016-7037\(94\)90269-0](https://doi.org/10.1016/0016-7037(94)90269-0), 1994.

1030 Wu, F. Y., Jahn, B. M., Wilde, S. A., Lo, C. H., Yui, T. F., Lin, Q., Ge, W. C., and Sun,  
1031 D. Y.: Highly fractionated I-type granites in NE China (I): geochronology and  
1032 petrogenesis, *Lithos*, 66, 241–273, [https://doi.org/10.1016/s0024-4937\(02\)00222-](https://doi.org/10.1016/s0024-4937(02)00222-0)  
1033 0, 2003.

1034 Wu, F. Y., Liu, X. C., Ji, W. Q., Wang, J. M., and Yang, L.: Highly fractionated granites:  
1035 Recognition and research, *Sci. China. Earth. Sci.*, 60, 1201–1219,

1036 <https://doi.org/10.1007/s11430-016-5139-1>, 2017.

1037 Wu, F. Y., Yang, J. H., and Liu, X. M.: Geochronological framework of the Mesozoic  
1038 granitic magmatism in the Liaodong Peninsula, Northeast China (in Chinese with  
1039 English abstract), *Geol. J. China. Univ.*, 11, 305–317, 2005b.

1040 Wu, F.Y., Han, R.H., Yang, J.H., Wilde, S. A., Zhai, M.G., and Park, S. C.: Initial  
1041 constraints on the timing of granitic magmatism in North Korea using U-Pb zircon  
1042 geochronology, *Chem. Geol.*, 238, 232–248,  
1043 <https://doi.org/10.1016/j.chemgeo.2006.11.012>, 2007.

1044 Wu, F.Y., Lin, J.Q., Wilde, S. A., Zhang, X.O., and Yang, J.H.: Nature and significance  
1045 of the Early Cretaceous giant igneous event in eastern China, *Earth. Planet. Sci.*  
1046 *Lett.*, 233, 103–119, <https://doi.org/10.1016/j.epsl.2005.02.019>, 2005c.

1047 Wu, F.Y., Yang, J.H., Wilde, S. A., and Zhang, X.O.: Geochronology, petrogenesis and  
1048 tectonic implications of Jurassic granites in the Liaodong Peninsula, NE China,  
1049 *Chem. Geol.*, 221, 127–156, <https://doi.org/10.1016/j.chemgeo.2005.04.010>,  
1050 2005a.

1051 Wu, F.Y., Yang, Y.H., Xie, L.W., Yang, J.H., and Xu, P.: Hf isotopic compositions of  
1052 the standard zircons and baddeleyites used in U-Pb geochronology, *Chem. Geol.*,  
1053 234, 105–126, <https://doi.org/10.1016/j.chemgeo.2006.05.003>, 2006.

1054 Xu, J. F., Shinjo, R., Defant, M. J., Wang, Q., and Rapp, R. P.: Origin of Mesozoic  
1055 adakitic intrusive rocks in the Ningzhen area of east China: partial melting of  
1056 delaminated lower continental crust? *Geology*, 30(12), 1111–1114,  
1057 [https://doi.org/10.1130/0091-7613\(2002\)0302.0.CO;2](https://doi.org/10.1130/0091-7613(2002)0302.0.CO;2), 2002.

- 1058 Xue, J. X., Liu, Z. H., Liu, J. X., Dong, X. J., Feng, F., and Lian, G. H.: Geochemistry,  
1059 Geochronology, Hf isotope and Tectonic Significance of the Late Jurassic Huangdi  
1060 Pluton in Xiuyan, Liaodong Penins (in Chinese with English abstract), Earth  
1061 Science, 46(6), 2030–2043, <https://doi.org/10.3799/dqkx.2020.008>, 2020.
- 1062 Xue, S., Ling, M. X., Liu, Y. L., Zhang, H., and Sun, W.D.: The genesis of early  
1063 Carboniferous adakitic rocks at the southern margin of the Alxa Block, North  
1064 China, *Lithos*, 278–281, 181–194, <https://doi.org/10.1016/j.lithos.2017.01.012>,  
1065 2017.
- 1066 Yang, F.C., Song, Y.H., Hao, L.B., and Peng, C.: Late Jurassic SHRIMP U-Pb age and  
1067 Hf isotopic characteristics of granite from the Sanjiazi Area in Liaodong and their  
1068 geological significance (in Chinese with English abstract), *Acta. Geol. Sin. Engl.*,  
1069 89, 1773–1782, 2015a.
- 1070 Yang, F.C., Song, Y.H., Yang, J.L., Shen, X., and Gu, Y.C.: SHRIMP U-Pb age and  
1071 geochemical characteristics of granites in Wulong-Sidaogou Gold Deposit, East  
1072 Liaoning (in Chinese with English abstract), *Geotectonica et Metallogenia*, 42,  
1073 940–954, <https://doi.org/10.16539/j.ddgzyckx.2018.05.010>, 2018.
- 1074 Yang, J. H., Wu, F. Y., Xie, L. W., and Liu, X. M.: Petrogenesis and tectonic  
1075 implications of Kuangdonggou synites in the Liaodong Peninsula, east North  
1076 China Craton: Constraints from in-suit zircon U-Pb ages and Hf isotopes (in  
1077 Chinese with English abstract), *Acta. Petrol. Sin.*, 23, 263–276,  
1078 <https://doi.org/10.1016/j.sedgeo.2006.03.028>, 2007.
- 1079 Yang, J.H., Wu, F.Y., Lo, C.H., Chung, S.L., Zhang, Y.B., and Wilde, S.A.:



1080 Deformation age of Jurassic granites in the Dandong area, eastern China: Ar-  
1081 40/Ar-39 geochronological constraints (in Chinese with English abstract), *Acta.*  
1082 *Petrol. Sin.*, 20(5), 1205–1214, 2004.

1083 Yang, M. C., Chen, B., and Yan, C.: Petrological, geochronological, geochemical and  
1084 Sr-Nd-Hf isotopic constraints on the petrogenesis of the Shuangcha  
1085 Paleoproterozoic megaporphyritic granite in the southern Jilin Province: Tectonic  
1086 implications (in Chinese with English abstract), *Acta. Petrol. Sin.*, 31, 1573–1588,  
1087 2015b.

1088 Yang, M.C., Chen, B., and Yan, C.: Paleoproterozoic Gneissic Granites in the Liaoji  
1089 Mobile Belt, North China Craton: Implications for Tectonic Setting. In: Zhai M.,  
1090 Zhao Y., Zhao T. (eds) *Main Tectonic Events and Metallogeny of the North China*  
1091 *Craton*, Springer. Geology. Springer. Singapore., 155–180,  
1092 [https://doi.org/10.1007/978-981-10-1064-4\\_7](https://doi.org/10.1007/978-981-10-1064-4_7), 2016.

1093 Yu, S., Zhang, J., and Del Real, P. G.: Geochemistry and zircon U-Pb ages of adakitic  
1094 rocks from the Dulan area of the North Qaidam UHP terrane, north Tibet:  
1095 constraints on the timing and nature of regional tectonothermal events associated  
1096 with collisional orogeny, *Gondwana. Res.*, 21, 167–179,  
1097 <https://doi.org/10.1016/j.gr.2011.07.024>, 2012.

1098 Yuan, H.L., Gao, S., Dai, M.N., Zong, C.L., Günther, D., Fontaine, G.H., Liu, X.M.,  
1099 and Diwu, C.R.: Simultaneous determinations of U-Pb age, Hf isotopes and trace  
1100 element compositions of zircon by excimer laser-ablation quadrupole and  
1101 multiple-collector ICP-MS, *Chem. Geol.*, 247, 100–118,

1102 <https://doi.org/10.1016/j.chemgeo.2007.10.003>, 2008.

1103 Yuan, L. L., Zhang, X. H., Xue, F. H., Han, C. M., Chen, H. H., and Zhai, M. G.: Two  
1104 episodes of Paleoproterozoic mafic intrusions from Liaoning province, North  
1105 China Craton: Petrogenesis and tectonic implications, *Precambrian. Res.*, 264,  
1106 119–139, <https://doi.org/10.1016/j.precamres.2015.04.017>, 2015.

1107 Zeng, R.Y., Lai, J.Q., Mao, X.C., Li, B., Ju, P.J., and Tao, S.L.: Geochemistry, zircon  
1108 U-Pb dating and Hf isotopies composition of Paleozoic granitoids in Jinchuan,  
1109 NW China: Constraints on their petrogenesis, source characteristics and tectonic  
1110 implication, *J. Asian. Earth. Sci.*, 121, 20–33,  
1111 <https://doi.org/10.1016/j.jseaes.2016.02.009>, 2016.

1112 Zeng, R.Y., Lai, J.Q., Mao, X.C., Li, B., Zhang, J.D., Bayless, R., and Yang, L.Z.:  
1113 Paleoproterozoic Multiple Tectonothermal Events in the Longshoushan Area,  
1114 Western North China Craton and Their Geological Implication: Evidence from  
1115 Geochemistry, Zircon U-Pb Geochronology and Hf Isotopes, *Minerals. Basel.*, 8,  
1116 <https://doi.org/10.3390/MIN8090361>, 2018.

1117 Zhai, M.G., Meng, Q.R., Liu, J.M., Hou, Q.L., Hu, S.B., Li, Z., Zhang, H.F., Liu, W.,  
1118 Shao, J.A., and Zhu, R.X.: Geological features of Mesozoic tectonic regime  
1119 inversion in eastern North China and implication for geodynamics, *Earth. Science.*  
1120 *Frontiers.*, 11, 285–298, <https://doi.org/10.3321/j.issn:1005-2321.2004.03.027>,  
1121 2004.

1122 Zhan, Q. Y., Zhu, D. C., Wang, Q., Weinberg, R. F., Xie, J. C., Li, S. M., Zhang, L.L.,  
1123 and Zhao, Z. D.: Source and pressure effects in the genesis of the Late Triassic

1124 high Sr/Y granites from the Songpan-Ganzi Fold Belt, eastern Tibetan Plateau,  
1125 Lithos, 368–369, <https://doi.org/10.1016/j.lithos.2020.105584>, 2020.

1126 Zhang, B., Guo, F., Zhang, X. B., Wu, Y.M., Wang, G.Q., and Zhao, L.: Early  
1127 Cretaceous subduction of Paleo-Pacific Ocean in the coastal region of SE China:  
1128 Petrological and geochemical constraints from the mafic intrusions, Lithos, 334–  
1129 335, 8–24, <https://doi.org/10.1016/j.lithos.2019.03.010>, 2019.

1130 Zhang, Q., Qian, Q., Wang, E.Q., Wang, Y., Zhao, T.P., Hao, J., and Guo, G.J.: An  
1131 East China plateau in mid-late Yanshanian period: implication from adakites,  
1132 Chinese (in Chinese with English abstract). Chinese Journal of Geology, 36 (2),  
1133 248–255, 2001.

1134 Zhang, Q., Wang, Y., Liu, H., and Wang, Y.: On the space-time distribution and  
1135 geodynamic environments of adakites in China annex: controversies over differing  
1136 opinions for adakites in China (in Chinese with English abstract), Earth Science  
1137 Frontiers, [https://doi.org/10.1016/S0955-2219\(02\)00073-0](https://doi.org/10.1016/S0955-2219(02)00073-0), 2003.

1138 Zhang, S., Zhu, G., Xiao, S.Y., Su, N., Liu, C., Wu, X.D., Yin, H., Li, Y.J., and Lu,  
1139 Y.C.: Temporal variations in the dynamic evolution of an overriding plate:  
1140 Evidence from the Wulong area in the eastern North China Craton, China, Geol.  
1141 Soc. Am. Bull., 132(9–10), 2023–2042, <https://doi.org/10.1130/B35465.1>, 2020.

1142 Zhao, K.D., Jiang, S.Y., Ling, H.F., and Palmer, M. R.: Reliability of LA-ICP-MS U-  
1143 Pb dating of zircons with high U concentrations: A case study from the U-bearing  
1144 Douzhashan Granite in South China, Chem. Geol., 389, 110–121,  
1145 <https://doi.org/10.1016/j.chemgeo.2014.09.018>, 2014.

- 1146 Zhao, K.D., Jiang, S.Y., Ling, H.F., and Palmer, M. R.: Reliability of LA-ICP-MS U-  
1147 Pb dating of zircons with high U concentrations: A case study from the U-bearing  
1148 Douzhashan Granite in South China, *Chem. Geol.*, 389, 110–121,  
1149 <https://doi.org/10.1016/j.chemgeo.2014.09.018>, 2014.
- 1150 Zheng, J.P., and Dai, H.K.: Subduction and retreating of the western Pacific plate  
1151 resulted in lithospheric mantle replacement and coupled basinmountain respond in  
1152 the North China Craton, *Sci. China. Earth. Sci.*, 61, 406–424,  
1153 <https://doi.org/10.1007/s11430-017-9166-8>, 2018.
- 1154 Zheng, Y.F., Xu, Z.F., Zhao, Z.F., and Dai, L.Q.: Mesozoic mafic magmatism in North  
1155 China: Implications for thinning and destruction of cratonic lithosphere, *Sci. China.  
1156 Earth Sci.*, 61, 353–385, <https://doi.org/10.1007/s11430-017-9160-3>, 2018.
- 1157 Zhu, R. X., and Xu, Y. G.: The subduction of the west Pacific plate and the destruction  
1158 of the North China Craton, *Sci. China. Earth Sci.*, 62, <https://doi.org/1340-1350>,  
1159 10.1007/s11430-018-9356-y, 2019.
- 1160 Zhu, R.X., and Xu, Y.G.: The subduction of the west Pacific plate and the destruction  
1161 of the North China Craton, *Sci. China. Earth. Sci.*, 62, 1340–1350,  
1162 <https://doi.org/10.1007/s11430-018-9356-y>, 2019.

1163 **Table captions**

1164 Table S1. Major element (wt. %) and trace element (ppm) compositions of the  
1165 Zhoujiapuzi granite

1166 Table S2. Raman microprobe data

1167 Table S3. The zircon major element (wt. %) and trace element (ppm) from the

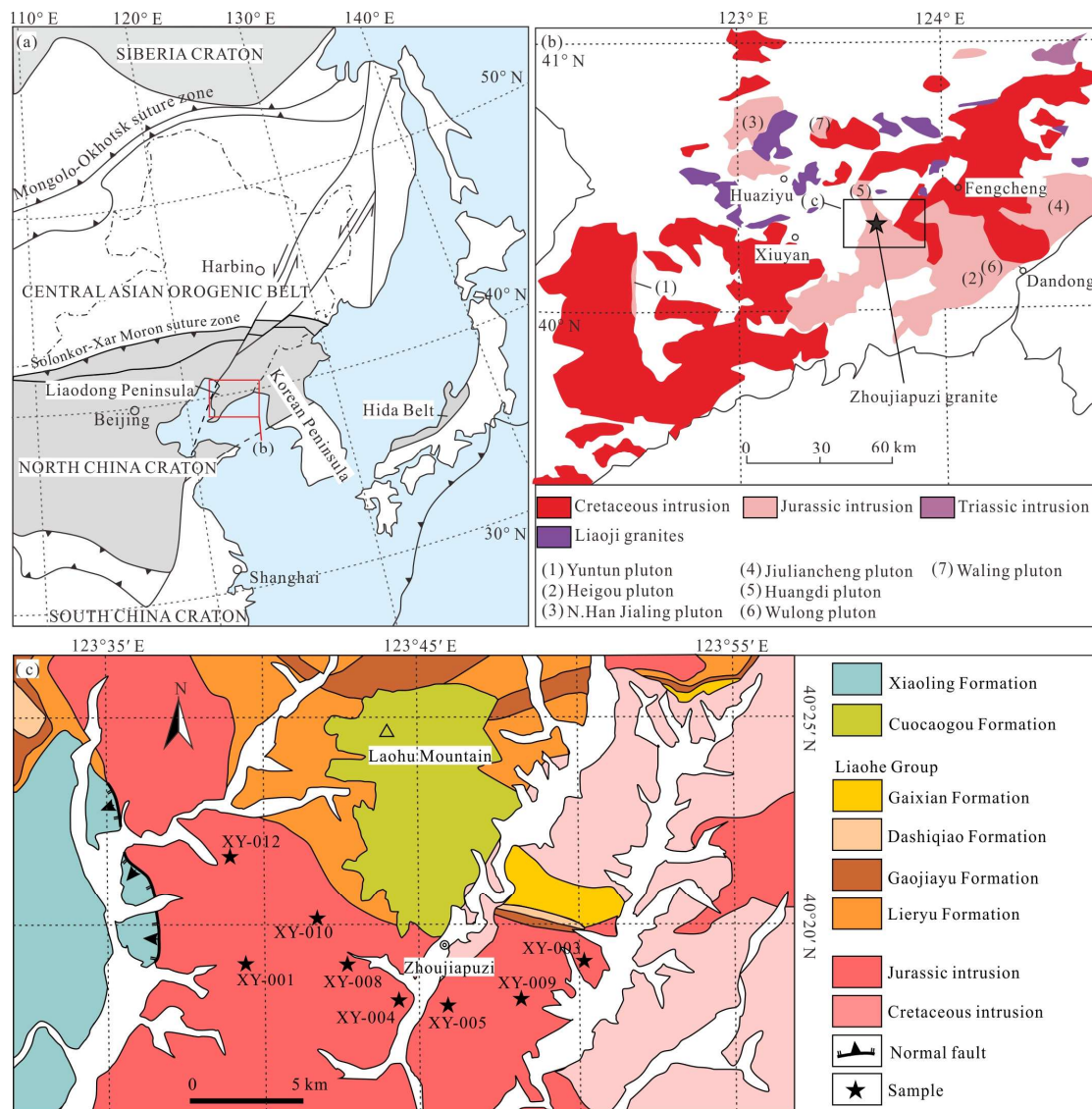
1168 Zhoujiapuzi granite

1169 Table S4. Zircon La-ICP-MS U-Pb isotopic data and ages of the Zhoujiapuzi granite

1170 Table S5. Zircon Hf isotopic data of the Zhoujiapuzi granite

1171

1172 **Figure captions**



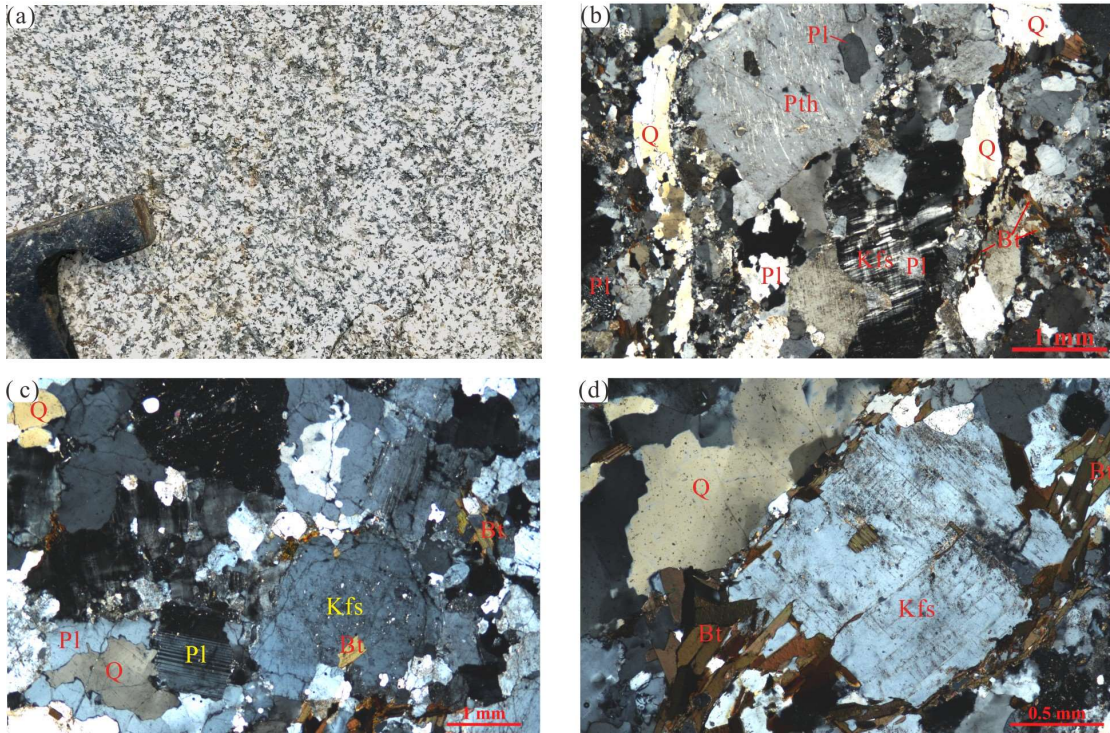
1173

1174 Figure 1. (a) Simplified geological map of Northeast China (Modified from Li et al.,

1175 2016); (b) distribution of Mesozoic intrusions in the Liaodong Peninsula (Modified

1176 from Wu et al., 2005a); (c) geological map of the Zhoujiapuzi granite.

1177



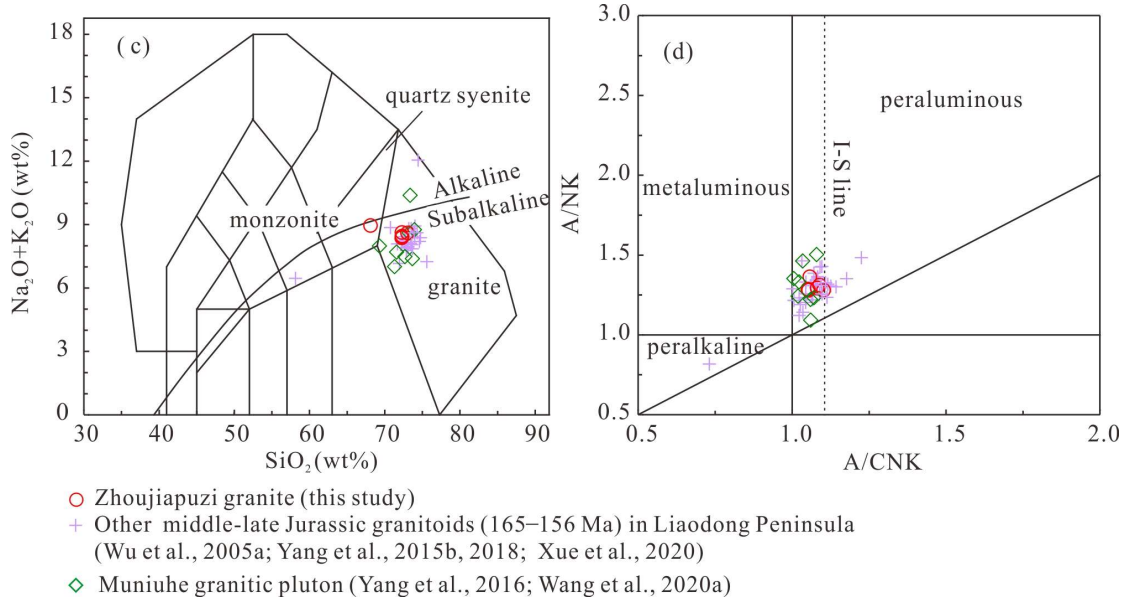
1178

1179 Figure 2. Outcrop photograph (a) and corresponding micrographs (b, c, d-

1180 perpendicular polarized light). Q quartz; Kfs feldspar; Pl plagioclase; Pth perthite; Bt

1181 biotite

1182



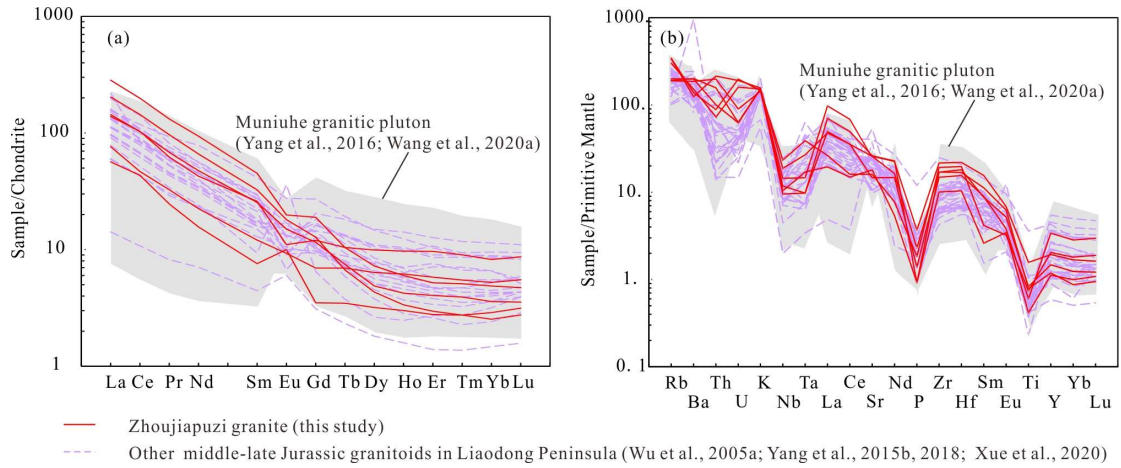
1183

1184 Figure 3. Geochemical classification diagrams for the Zhoujiapuzi granite. (a) TAS

1185 diagram (after Frost et al., 2001); (b) A/CNK-A/NK diagram (after Maniar and

1186 Piccoli, 1989)

1187



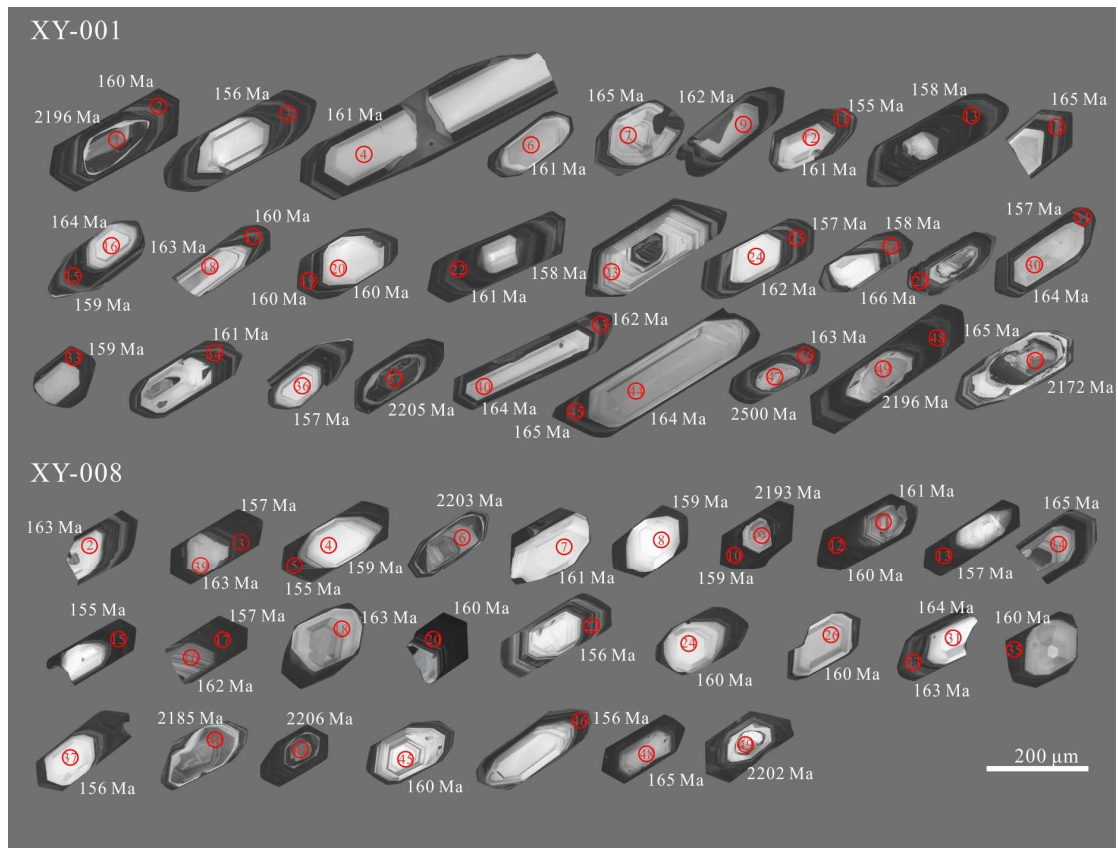
1188

1189 Figure 4. Chondrite-normalized REE patterns and primitive mantle-normalized trace

1190 element patterns of the Zhoujiapuzi granite (chondrite and primitive mantle values are

1191 from Sun and McDonough, 1989).

1192

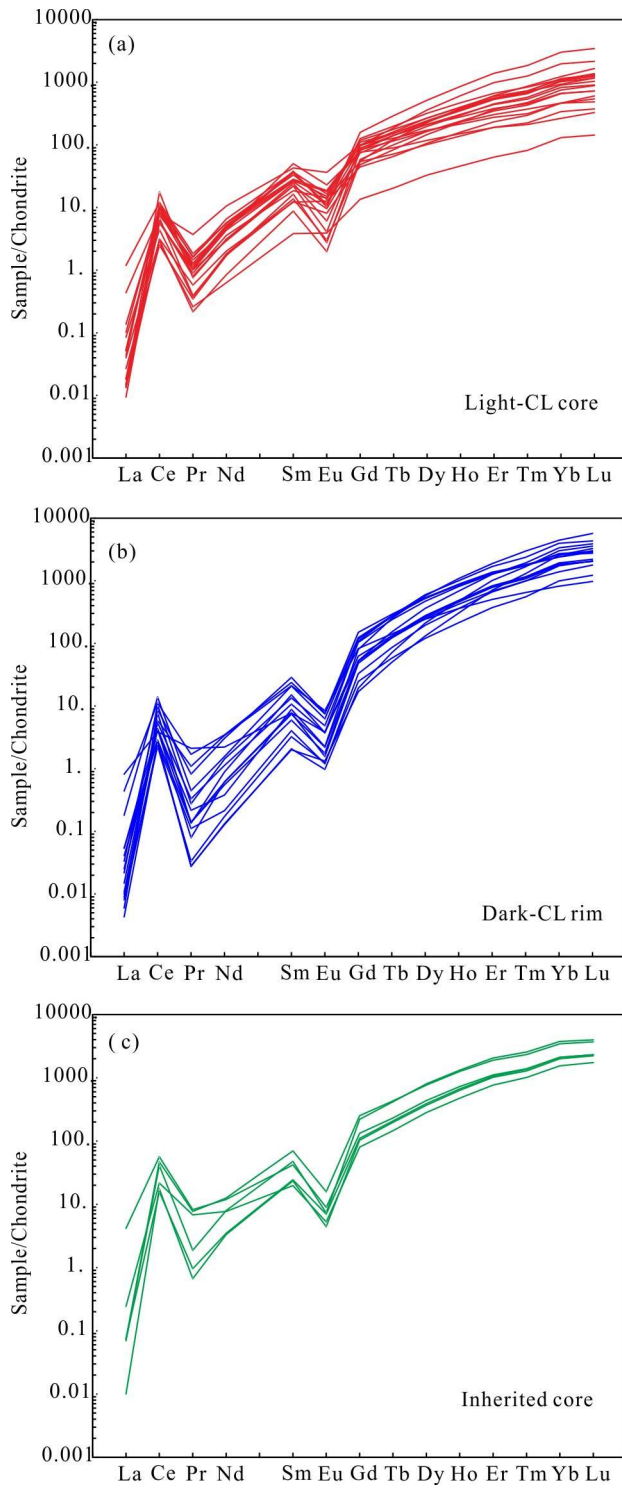


1193

1194 Figure 5. CL images of zircons. Circles denote U-Pb analysis spot. Numbers in the  
 1195 circles are the spot numbers. Numbers near the analytical spots are the U-Pb ages  
 1196 (Ma).

1197



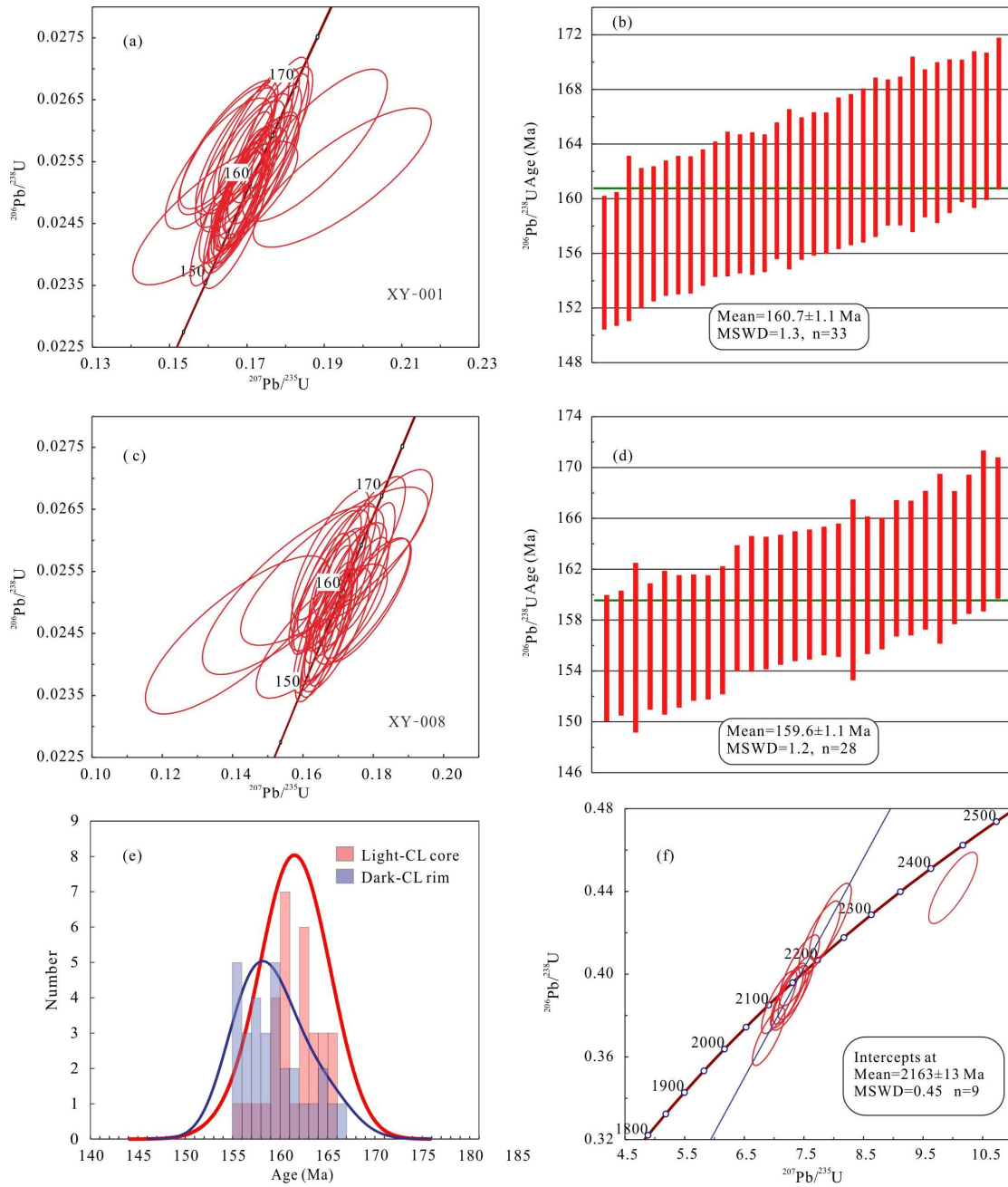


1198

1199 Figure 6. Chondrite-normalized REE patterns of zircon (chondrite values are from

1200 Sun and McDonough, 1989).

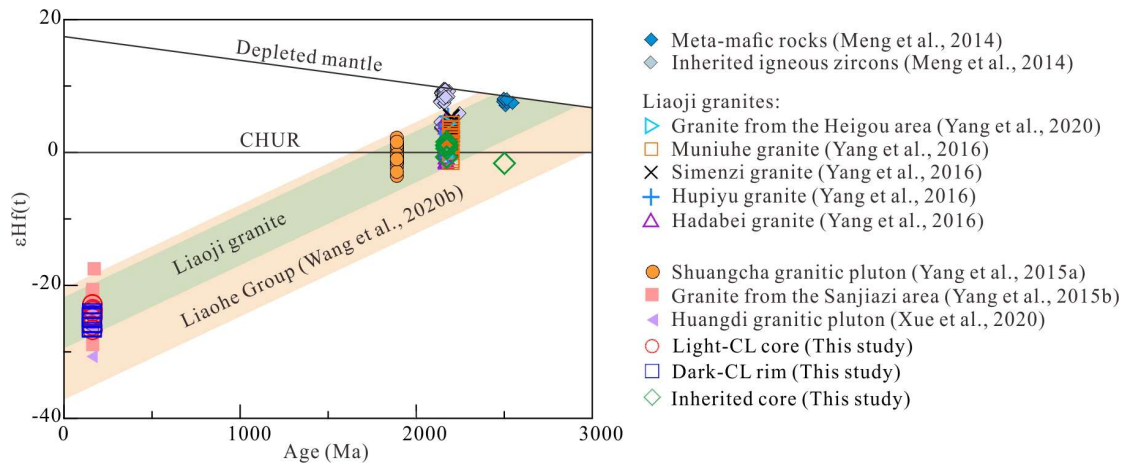
1201



1202

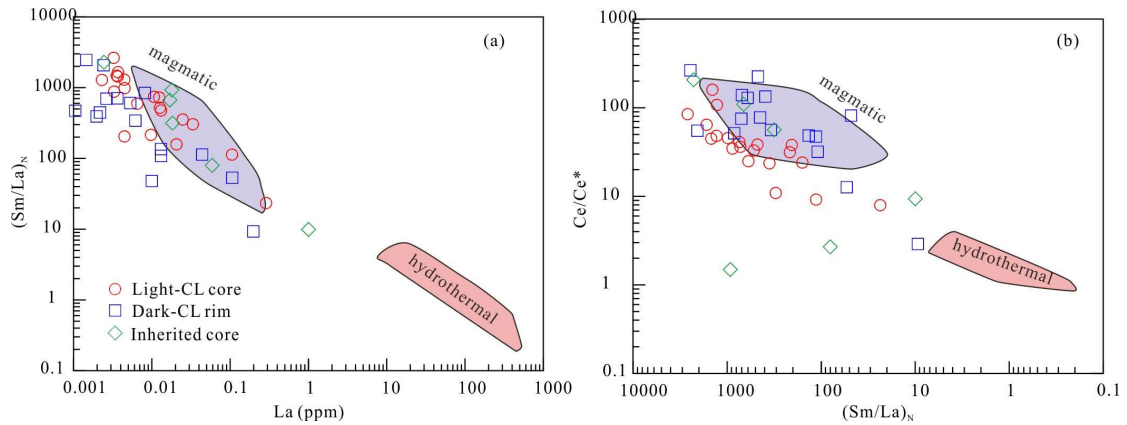
1203 Figure 7. Concordia diagrams for zircon LA-ICP-MS U-Pb analyses.

1204



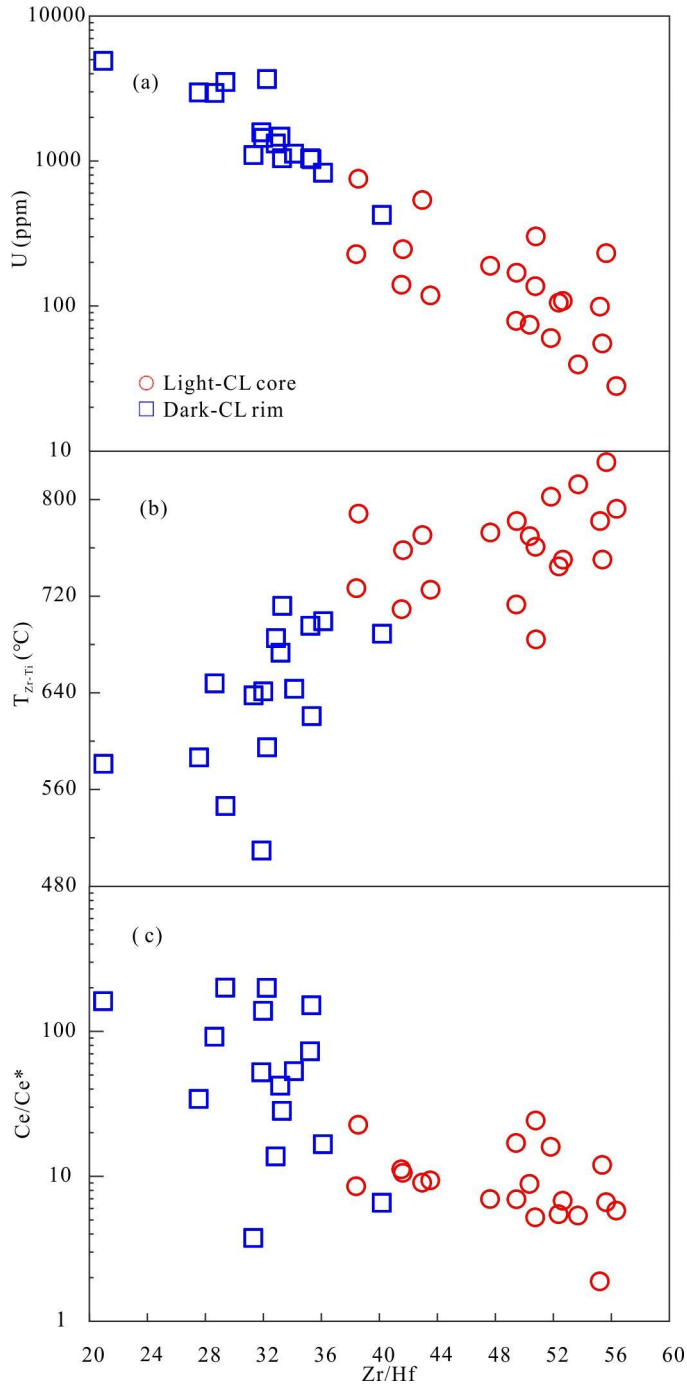
1205  
 1206 Figure 8. Zircon  $\epsilon\text{Hf}(t)$ -age (Ma) diagram for samples in this study and published data  
 1207 for the region.

1208



1209  
 1210 Fig. 9. Discrimination plots for magmatic and hydrothermal zircon (Hoskin, 2005).

1211

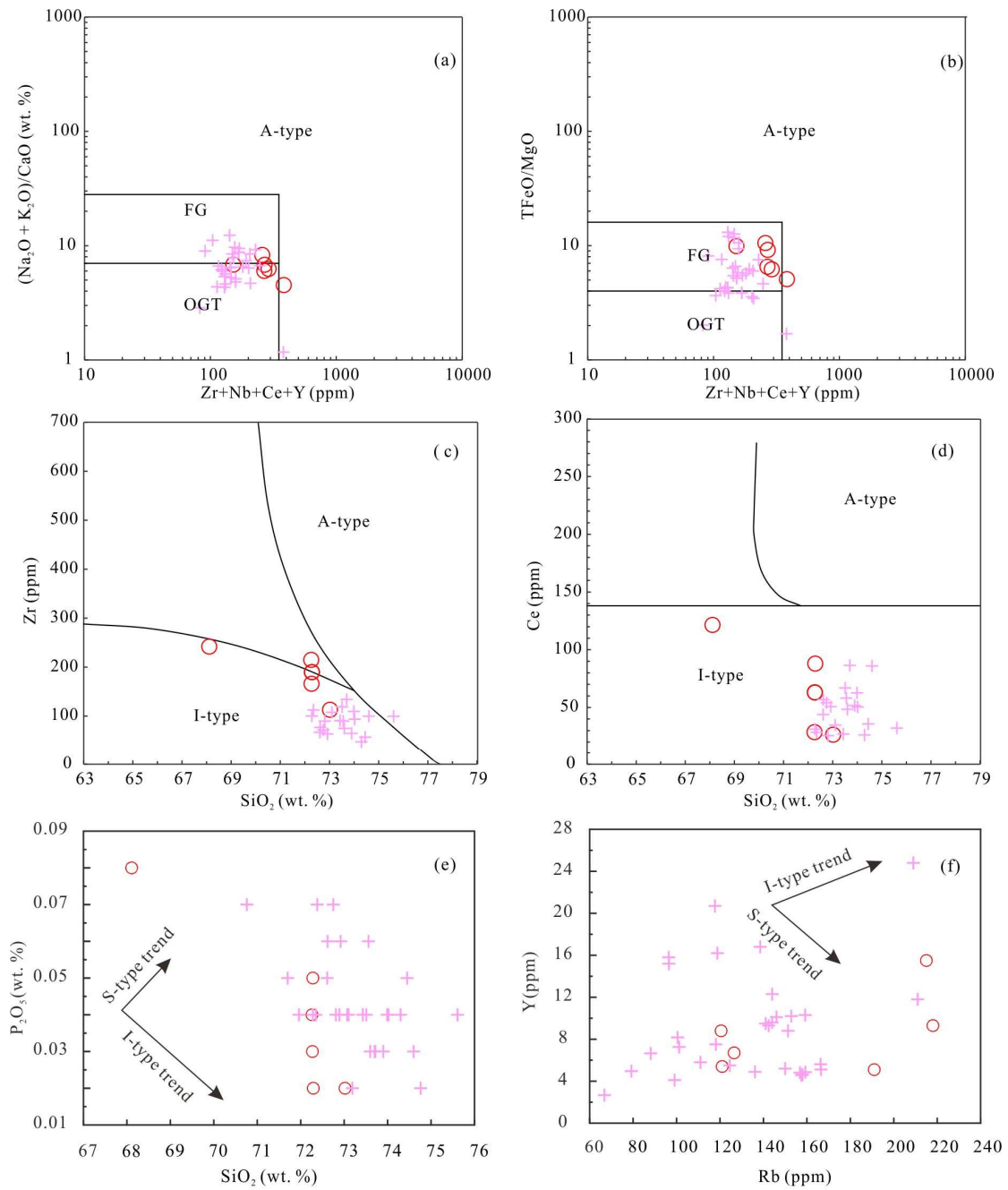


1212

1213 Figure 10. Covariation diagrams for zircon from the Zhoujiapuzi granite. (a) U vs.

1214 Zr/Hf; (b)  $T_{Zr-Ti}$  vs. Zr/Hf; (c) Ce/Ce\* vs. Zr/Hf.

1215



○ Zhoujiapuzi granite (this study)

+ Other middle-late Jurassic granitoids in Liaodong Peninsula (Wu et al., 2005a; Yang et al., 2015b, 2018; Xue et al., 2020)

1216

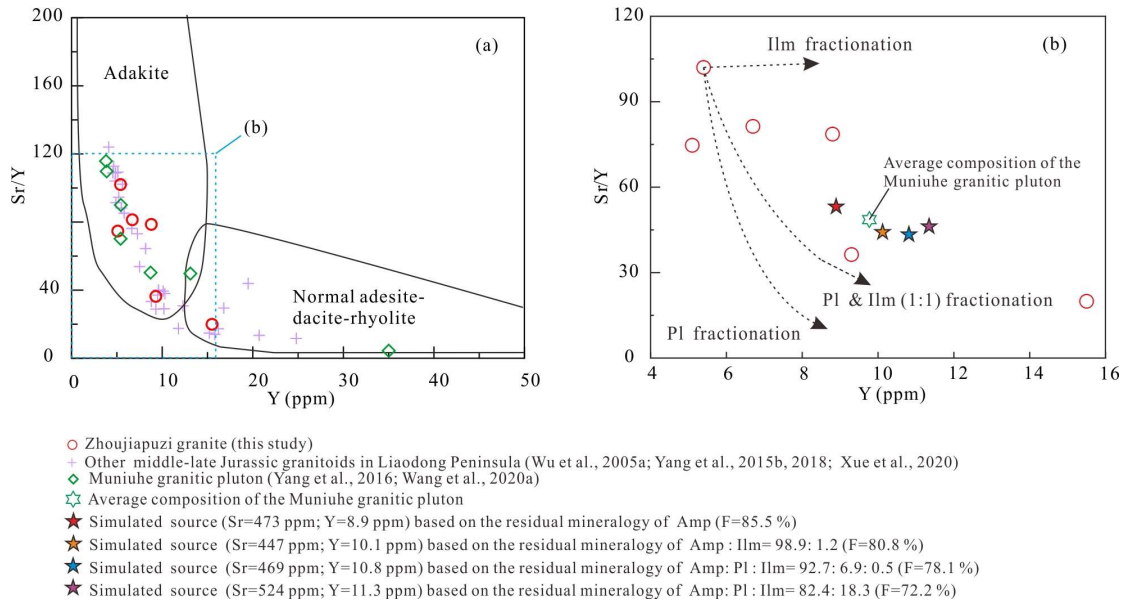
1217 Figure 11. Chemical variation diagrams for the Zhoujiapuzi granite. (a and b)

1218  $\text{Zr} + \text{Nb} + \text{Ce} + \text{Y}$  vs.  $(\text{Na}_2\text{O} + \text{K}_2\text{O})/\text{CaO}$  and  $\text{TFeO}/\text{MgO}$  (after Whalen et al., 1987); (c

1219 and d)  $\text{SiO}_2$  vs. Zr and Ce (after Collins et al., 1982); (e)  $\text{SiO}_2$  vs.  $\text{P}_2\text{O}_5$  diagram; (f)

1220 Rb vs. Y diagram

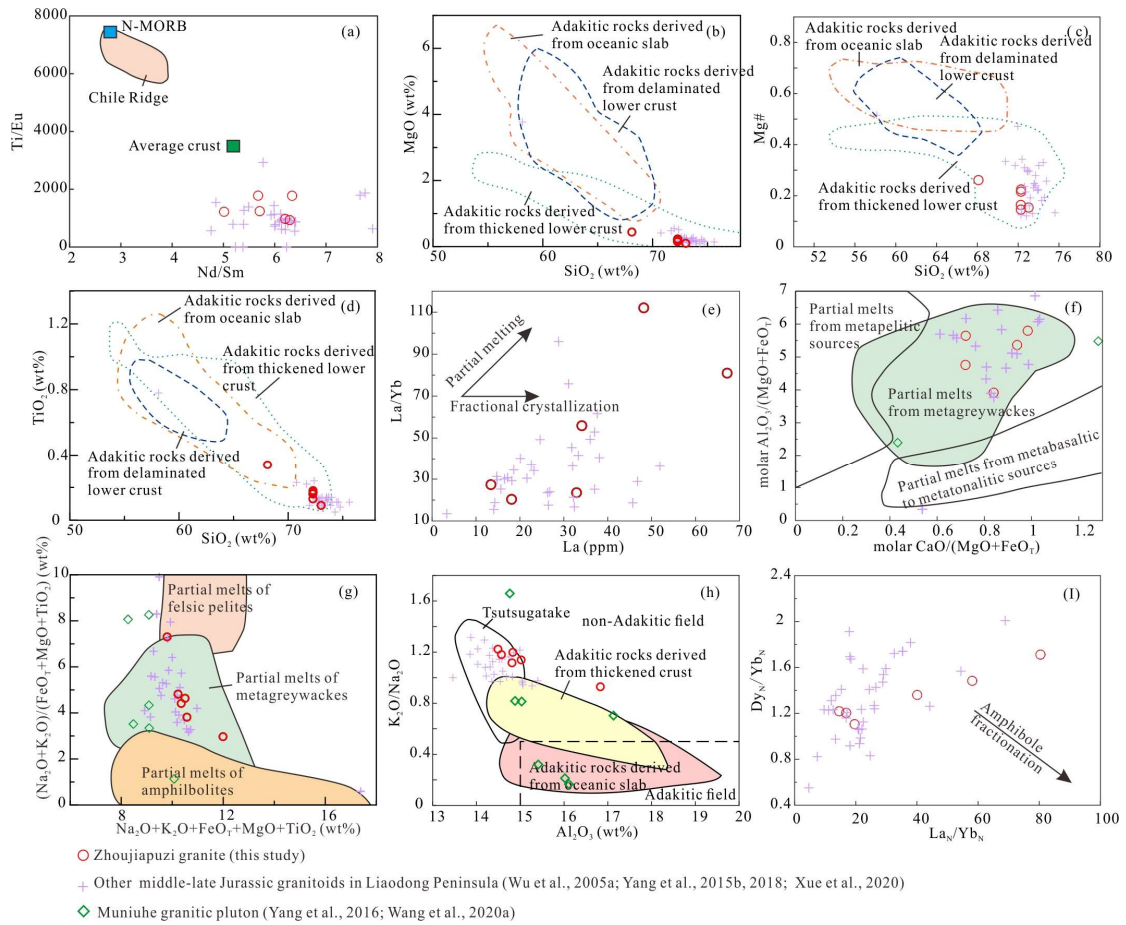
1221



1222

1223 Figure 12. Adakite discrimination diagrams for the Zhoujiapuzi granite (after Defant  
 1224 and Drummond, 1990).

1225

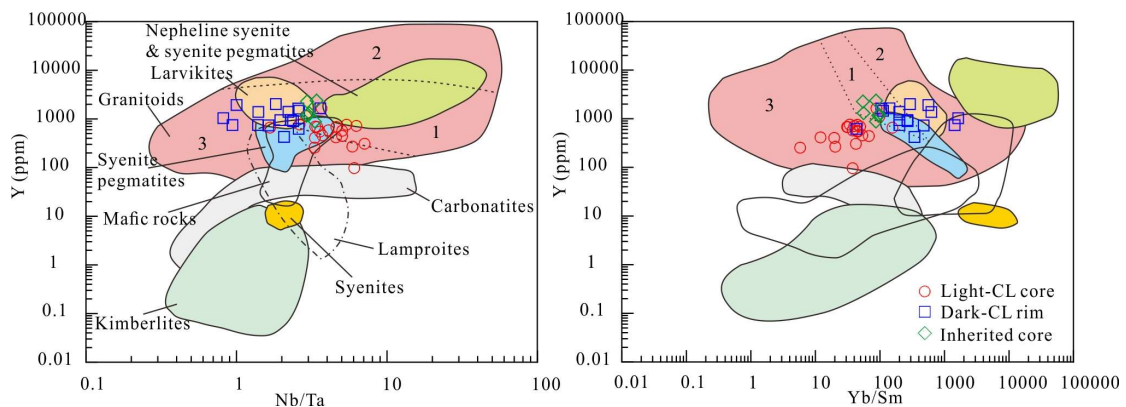


1226

1227 Figure 13. Source characteristics (a-d and f-h) and crystal fractionation (e and i)

1228 discrimination diagrams for the Zhoujiapuzi granite. Plots of (a) Nd/Sm vs. Ti/Eu (Yu  
 1229 et al., 2012); (b-d) SiO<sub>2</sub> vs. MgO, Mg# and TiO<sub>2</sub> (after Wang et al., 2006); (e) La vs.  
 1230 La/Yb (Gao et al., 2007); (f) molar Al<sub>2</sub>O<sub>3</sub>/(MgO+FeO<sub>T</sub>) vs. molar CaO/(MgO+FeO<sub>T</sub>)  
 1231 (after Altherr et al., 2000); (g) (Na<sub>2</sub>O+K<sub>2</sub>O)/(FeO<sub>T</sub>+MgO+TiO<sub>2</sub>) vs.  
 1232 Na<sub>2</sub>O+K<sub>2</sub>O+FeO<sub>T</sub>+MgO+TiO<sub>2</sub> (after Patiño Douce, 1999); (h) K<sub>2</sub>O/Na<sub>2</sub>O vs. Al<sub>2</sub>O<sub>3</sub>  
 1233 diagrams (after Kamei et al., 2009); (i) La<sub>N</sub>/Yb<sub>N</sub> vs. Dy<sub>N</sub>/Yb<sub>N</sub>.

1234



1235

1236 Figure 14. The fields of zircon compositions used as discriminants for different rock  
 1237 types (after Belousova et al., 2002). ‘Granitoids’ include: 1 aplites and leucogranites;  
 1238 2 granites; 3 granodiorites and tonalities

1239

1240